

**A COMPREHENSIVE ANALYSIS OF GaN HEMTs:
ELECTRO-MECHANICAL BEHAVIOR, DEFECT
GENERATION, AND DRAIN LAG REDUCTION
WITH HfO₂ LAYERS**

A THESIS SUBMITTED TO
THE GRADUATE SCHOOL OF ENGINEERING AND SCIENCE
OF BILKENT UNIVERSITY
IN PARTIAL FULFILLMENT OF THE REQUIREMENTS FOR
THE DEGREE OF
MASTER OF SCIENCE
IN
ELECTRICAL AND ELECTRONICS ENGINEERING

By
Burak Güneş
July 2023

A Comprehensive Analysis of GaN HEMTs: Electro-mechanical Behavior,
Defect Generation, and Drain Lag Reduction with HfO₂ Layers

By Burak Güneş

July 2023

We certify that we have read this thesis and that in our opinion it is fully adequate, in scope and in quality, as a thesis for the degree of Master of Science.

Ekmel Özbay(Advisor)

Bayram Bütün(Co-Advisor)

Abdullah Atalar

Sefer Bora Lişesivdin

Approved for the Graduate School of Engineering and Science:

Orhan Arıkan
Director of the Graduate School

ABSTRACT

A COMPREHENSIVE ANALYSIS OF GaN HEMTs: ELECTRO-MECHANICAL BEHAVIOR, DEFECT GENERATION, AND DRAIN LAG REDUCTION WITH HfO₂ LAYERS

Burak Güneş

M.S. in Electrical and Electronics Engineering

Advisor: Ekmel Özbay

Co-Advisor: Bayram Bütün

July 2023

Gallium Nitride High Electron Mobility Transistors (GaN HEMTs) have rapidly emerged as a transformative technology, owing to the unique properties of the substrate material. They are poised to become a revolutionary advancement in RF amplifier applications, primarily due to their capability to operate at high frequencies and power levels with superior efficiency compared to conventional devices. Despite the rapid progressions, a noticeable gap persists in the literature regarding the relationship between mechanical stresses, defect generation, and their subsequent impact on the electrical characteristics of AlGaN/GaN HEMTs. Moreover, current dispersion effects, which are trapping induced reductions in output power, continues to remain a pressing issue. To address these limitations, this study first adopts a multifaceted approach and integrates mechanical simulations and Raman spectroscopy, in order to resolve fine details of stress distributions that a diffraction-limited Raman probe cannot resolve. This enables an extensive modeling of stresses in a typical HEMT structure and helps elucidate the underlying dynamics of defect generation, with the ultimate goal of informing and guiding the development of advanced fabrication techniques. In a second study, an ultrathin blanket dielectric deposition approach was devised to alleviate surface trapping, and consequently, mitigate current dispersion. The proposed streamlined fabrication process yielded a substantial improvement in device performance without compromising the transistor transfer characteristics.

Keywords: GaN HEMT, Electro-mechanical Simulations, Defect Generation, Electrical Stability, Raman Spectroscopy, Electron Traps.

ÖZET

GaN YEMT'LERİN KAPSAMLI BİR ANALİZİ: ELEKTRO-MEKANİK DAVRANIŞ, KUSUR OLUŞUMU VE HfO₂ KATMANLARI İLE ELEKTRİKSEL KARARLILIĞIN İYİLEŞTİRİLMESİ

Burak Güneş

Elektrik ve Elektronik Mühendisliği, Yüksek Lisans

Tez Danışmanı: Ekmel Özbay

İkinci Tez Danışmanı: Bayram Bütün

Temmuz 2023

GaN temelli yüksek-elektron-mobiliteli transistörler (GaN YEMT) geleneksel cihazlara kıyasla üstün verimlilikle yüksek frekanslarda ve güç seviyelerinde çalışabilme yetenekleri nedeniyle yükselteç uygulamalarında devrim niteliğinde ilerlemelerin yolunu açıyorlar. Tüm gelişmelere karşın mekanik stresler, kristal üzerinde kusur oluşumu ve bunların GaN YEMT'lerin elektriksel özellikleri üzerindeki etkileri arasındaki ilişkiler hakkında literatürde belirgin bir boşluk bulunmaktadır. Ayrıca yükselteç çıkış gücündeki tuzaklama temelli azalmalar bir sorun olmaya devam etmektedir. Bu çalışmada belirtilen sınırlamaları gidermek için ilk olarak çok yönlü bir yaklaşım benimsenmiş ve Raman spektroskopisi ölçümlerini mekanik simülasyonlar için bir kalibrasyon referansı olarak kullanılmış, bu da bir kısımla sınırlı Raman probunun çözümlenemeyeceği stres dağılımlarının ince ayrıntılarını gözlemlemeyi sağlamıştır. Bu yaklaşım, tipik bir YEMT yapısındaki mekanik stresleri modellemeyi sağlamaktadır ve kusur oluşumunun altında yatan dinamikleri aydınlatmaya yardımcı olmaktadır. Bu yaklaşımla fabrikasyon tekniklerinin geliştirilmesini hedeflemektedir. Çalışmanın devamında yüzey tuzaklamasını azaltmak için ince bir yalıtkan malzeme kaplama yaklaşımı tasarlanmıştır. Önerilen üretim süreci, transistör transfer karakteristiklerini kötüleştirmeden cihaz performansında önemli bir gelişme sağlamıştır.

Anahtar sözcükler: GaN, YEMT, Elektro-mekanik Simülasyonlar, Kusur Oluşumu, Elektriksel Kararlılık, Raman Spektroskopisi, Elektron Tuzakları.

Acknowledgement

I am deeply grateful to my advisor, Prof. Ekmel Özbay, for his kindness, promptness, and immense patience throughout this journey. His constant support has been invaluable.

My sincere appreciation goes to my co-advisor, Dr. Bayram Bütün. His academic guidance was always enlightening, and our meetings were not only filled with insights but they were also instrumental in supporting my personal growth.

I am thankful to the members of the thesis committee, Prof. Abdullah Atalar and Prof. Sefer Bora Lişesivdin, for their valuable time.

Special thanks to Dr. Amir Ghobadi for our research discussions and to Oğuz Odabaşı for his invaluable clean room trainings. I am also grateful to the members of ABMN and NANOTAM for their assistance in clean room fabrication and device measurements.

I would like to acknowledge the financial contributions from Turkcell Technology, Information and Communication Technologies Authority (BTK), TÜBİTAK, NANOTAM, and Bilkent University.

Lastly, I would also like to express my heartfelt gratitude to my family. To my parents, Nevin and Hüseyin, and to my sister, Melike, for their constant encouragement and unwavering support.

Contents

- 1 Introduction** **1**
 - 1.1 Thesis Outline 2

- 2 Electrical, Solid-mechanics, and Electro-mechanical GaN HEMT Simulations** **4**
 - 2.1 Electrical Simulations 4
 - 2.1.1 Overview of the Simulation Model 5
 - 2.1.2 Buffer Traps 6
 - 2.1.3 Density-dependent Electron Mobility Model Development . . 11
 - 2.2 Solid-mechanics Simulations 15
 - 2.2.1 Overview of the Simulation Model 15
 - 2.2.2 Stress Definitions 18
 - 2.3 Uncoupled Electro-mechanical Simulations 20
 - 2.3.1 Calculation of Polarization Induced Bound Charges 20

2.3.2 Electro-mechanical Simulation Workflow 21

2.3.3 Case Study 22

3 Analysis and Modeling of Mechanical Stresses in Ungated AlGaN/GaN HEMTs using μ Raman Spectroscopy 26

3.1 Motivation 26

3.2 Experimental Methodology 28

3.2.1 Ungated HEMTs 28

3.2.2 μ Raman Spectroscopy 29

3.3 Results and Discussion 34

3.3.1 Measurement Results and Analysis 34

3.3.2 Simulation Model Calibration 35

3.3.3 Identifying Potential Defect Generation Spots using the Calibrated Mechanical Model 37

3.3.4 Impact of Defect Generation on Device Performance 43

3.4 Summary 45

4 Improved Drain Lag by Reduced Surface Current in GaN HEMT via an Ultrathin HfO₂ Blanket Layer 47

4.1 Motivation 47

4.2 Device Fabrication 50

4.3 Results and Discussion 52

CONTENTS

viii

4.4 Summary 60

5 Conclusions and Future Work 61

List of Figures

2.1	TEM image of a GaN HEMT.	5
2.2	Simulation model of a GaN HEMT constructed using the ATHENA software.	6
2.3	Two-dimensional schematic depicting the placement of bound charges, critical to the formation of the 2DEG.	7
2.4	Plot illustrating the distribution of doping and impurity concentrations.	8
2.5	Graphic representation of the energy levels associated with impurities and point defects.	9
2.6	Band diagram of the simulated AlGaIn/GaN heterojunction.	10
2.7	Breakdown simulation results depicting the current density and the onset of punch-through phenomenon.	11
2.8	Distribution of 2DEG density without considering the quantization effects on the density of states.	13
2.9	Calibration results compared to the measurement data reported in References 24 (a) and 25 (b).	15

2.10	Three-dimensional simulation model. Boundary conditions associated with surfaces are displayed with symbols.	16
2.11	Illustration of the impact of strain relaxation on bound charge density.	22
2.12	Two-dimensional depiction of the fin simulation model analyzed using COMSOL simulations.	23
2.13	Distribution of barrier strain in relation to fin width. Two boundary condition cases were studied. a) shows the results from the free top surface boundary condition case, whereas b) illustrates the impact of a fixed top surface boundary condition.	24
2.14	Average strain as a function of fin width.	24
2.15	Variation of 2DEG distribution with respect to fin width. Two boundary condition cases were studied. a) shows the results from the free top surface boundary condition case, whereas b) illustrates the impact of a fixed top surface boundary condition. Strain distribution results displayed in Figure 2.13 were converted to polarization charges by following the workflow explained in Section 2.3.1. Then, ATLAS calculated the resulting 2DEG densities and distributions.	25
2.16	Average 2DEG density as a function of fin width.	25
3.1	Cross-sectional view of the devices. The laser beam was focused onto the center of two ohmic contacts. The fine focus was accomplished by adjusting the z-axis position of the microscope objective.	28
3.2	Integrated Raman counts were maximized for tight focus. Inset: Raman spectra were integrated within $(550, 575) \text{ cm}^{-1}$. The shaded area represents the integration range.	30
3.3	Knife-edge lateral resolution measurement results of the optical setup and Gaussian cumulative distribution function fit.	31

3.4	Top view of the devices. Ten consecutive measurements were taken from the center of the devices.	32
3.5	Raman spectra were deconvolved into E_2 and E_1 line functions to locate the peak positions of the E_2 mode. One such deconvolution is shown.	32
3.6	E_2 mode peak position measurement results as a function of the pattern length. Error bars represent 99% CI from 10 measurements.	33
3.7	Frequency shifts of the E_2 and A_1 modes. Linear fit demonstrated the biaxiality of the measured stress modes.	33
3.8	Stress measurements and simulation model results. Stresses were calculated from the E_2 peak positions. Error bars represent 99% CI.	34
3.9	Data post-processing regions. Data from Region 1-3 were integrated along the wafer growth direction and reported as line plots. Line 1 represents the line-scan data acquisition 1 nm away from the hetero-junction interface.	39
3.10	Simulation results. Stress results from a) Region 1 and b) Line 1.	41
3.11	Elastic energy in the AlGaIn barrier. Energy levels required for the generation of channeling and surface cracks are also given.	42
3.12	A 2D simulation settings illustration depicting channeling cracks near the ohmic contacts.	43
3.13	TLM emulation results in relation to the severity of defect-induced relaxation	44
3.14	Extracted contact resistances from the emulated TLM results.	45

4.1	(a) Cross-section of the HEMTs (the reference sample is absent of the HfO ₂ layer). (b) Simplified fabrication flow.	51
4.2	Calculated conduction band diagram of the AlGaN/GaN HEMT gate stacks with and without the HfO ₂ dielectric.	51
4.3	Double pulsed measurement results. Insets of (a) and (b) show the drain lag results in close-up.	52
4.4	(a) and (b) display the cross-section of the devices used in the surface leakage current measurements. (a) also shows the measurement circuit for surface leakage current.	54
4.5	(a) Surface current measurement results. (b) Schottky leakage measurement results from the HEMTs.	54
4.6	(a) and (b) are the two-way I _D -V _G and I _G -V _G results of the transistors.	56
4.7	(a) I _D -V _D sweep at gate voltages ranging from -6 V to 0 V with 1 V steps. (b) Transconductance g _m at V _D = 10 V.	56
4.8	Current-controlled I _D -V _D measurements.	57
4.9	Conductance method results.	58
4.10	(a) The calculated interface trap density and (b) time constant evolution with gate voltage.	59
4.11	f _T as a function of gate bias at a fixed drain voltage of 10 V of (a) the reference and (b) HfO ₂ deposited transistors.	59

List of Tables

2.1	Explanation and details of the proposed calibration procedure.	14
2.2	Transistor geometry, reported results, and simulation model outputs. .	14
2.3	Elastic properties of the anisotropic simulation materials.	17
2.4	Elastic properties of the ohmic contact simulation material. Young’s Modulus of the ohmic contact material was calculated from the material constants of Ti, Al, Ni, and Au.	17
2.5	Stress-free lattice parameters used in the calculation of the barrier strain.	18
3.1	Proportionality constants and stress-free reference frequency used in the stress calculations.	31
3.2	Values of the stress and strain variables used in the simulation model.	36
4.1	Comparisons of MIS-HEMTs and MOS-HEMTs with the conventional Schottky-gate AlGaIn/GaN HEMTs.	53

Chapter 1

Introduction

Gallium Nitride (GaN) High Electron Mobility Transistors (HEMTs) have attracted significant attention in the field of electronics due to their superior performance in high-frequency and high-power applications. Central to this high performance is the formation of a two-dimensional electron gas (2DEG) at the heterointerface of AlGa_N and GaN layers in these devices [1]. The 2DEG, essentially a thin layer of electrons, is formed due to the polarization difference between AlGa_N and GaN materials [2]. This polarization-induced electric field leads to a very large concentration of electrons at the interface, thereby enabling a remarkable device performance. The absence of doping-induced scattering centers in the 2DEG channel further enhances the mobility, and consequently, the speed and efficiency of GaN HEMTs [3].

In recent years, GaN HEMTs have facilitated substantial technological advancements in wireless communications, radar systems, satellite technology, and power electronics. They have achieved record performances in terms of power density and efficiency, and their high breakdown field strength makes them ideal candidates for high voltage applications. For example, research by Fitch *et al.* reports devices with power densities exceeding 7 W/mm at 35 GHz [4]. Power-added efficiency values of 40% or more are consistently reported in the literature [5, 6]. Moreover, devices with current gain cut-off frequencies as high as 450 GHz have been documented [7].

However, certain limitations hinder this technology's broader implementation. Notably, the electrical stability and reliability of these devices remain subjects of significant concern. Phenomena such as current collapse, threshold voltage shifts, and breakdown are often observed under high electric field or high temperature operations [8, 9]. These effects can significantly degrade the performance and lifetime of the devices. Additionally, the 2DEG formation process is inherently sensitive to the variations in the structural properties of the devices. In particular, the fabrication-induced defects and strain relaxation phenomena can cause substantial variations in the 2DEG density [10]. A thorough understanding of these factors, along with the development of accurate simulation models, is essential to further take advantage of the potential of GaN HEMTs.

1.1 Thesis Outline

This thesis aims to further the understanding and optimization of GaN HEMTs. To this end, the research was organized into three objectives, each corresponding to a chapter of this work:

- Chapter 2 explores the creation of advanced simulation models. Special emphasis was placed on the development of electro-mechanical models. This effort involved not only the detailed simulation of electronic and transport characteristics but also the mechanical strain and stress effects that significantly influence the 2DEG formation and device performance.
- Chapter 3 offers a novel approach to integrating Raman measurements into mechanical simulations. This methodology provides a calibration reference to the simulations, enabling a detailed investigation into defect generation and its implications for GaN HEMT performance. This approach paves the way for a more comprehensive understanding of the structural complexities and their impact on the electrical behavior of the devices.
- Chapter 4 investigates the role of HfO₂ ultrathin gate dielectrics in improving

drain lag characteristics. This chapter explores the advantages of implementing HfO_2 as a blanket layer, elucidating its effects on device stability and the reduction of detrimental current dispersion effects.

- Finally, in Chapter 5, we summarize and discuss the achievements of this thesis, the proposed innovations, and contributions to the existing literature. Moreover, we outline future areas of research, which we anticipate will further deepen our understanding of the GaN HEMTs.

Chapter 2

Electrical, Solid-mechanics, and Electro-mechanical GaN HEMT Simulations

The presented simulation results and methodologies in this chapter were instrumental in setting the direction of the research. Although some of the arguments discussed here did not directly contribute to the main body of the thesis, they served to refine our understanding of GaN HEMTs and provided invaluable insights.

2.1 Electrical Simulations

This section delineates the electrical simulation methodologies utilized in this study. It begins with an overview of the simulation model, followed by an examination of the effects of both unintentional contaminants and deliberately introduced electron traps. The section concludes with a discussion on an innovative electron mobility model designed to augment the predictive capabilities of the simulation studies.

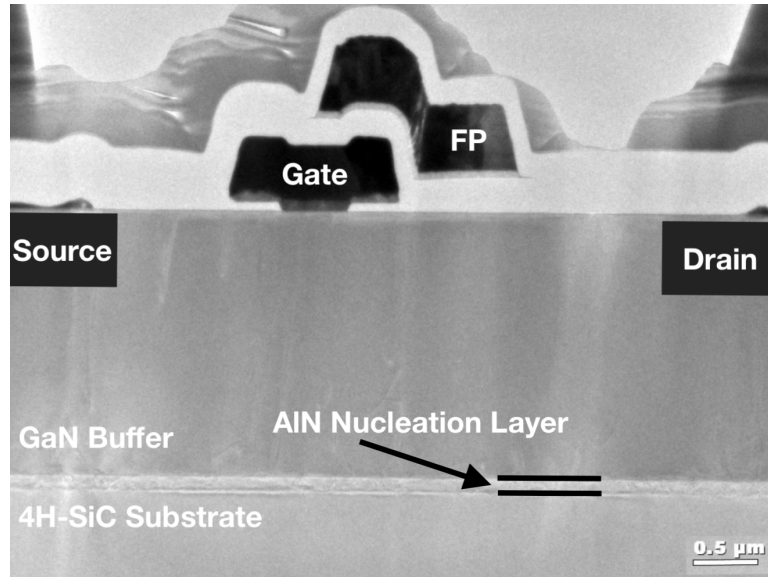


Figure 2.1: TEM image of a GaN HEMT.

2.1.1 Overview of the Simulation Model

The electrical simulation models were formulated in Silvaco ATLAS [11], which is a drift-diffusion based semiconductor device analysis program. Two-dimensional representations of the devices were established using Silvaco ATHENA [12], a process simulation program that enables the creation of accurate renditions of the actual device geometry. In particular, ATHENA makes it possible to model the influence of fabrication features and non-idealities such as sharp edges around the field plates, slanted sidewalls of the gate electrode, and uneven step coverage of the nitride passivation film. The actual device image captured using a transmission-electron microscope (TEM) is given in Figure 2.1. For comparison, a typical simulation geometry rendered in ATHENA is displayed in Figure 2.2.

To recreate the formation of 2DEG charges in simulations, bound charges were introduced along the AlGaN/GaN interface, as shown in Figure 2.3. The density of the interface charges were adjusted to align with the actual 2DEG density as determined from contactless measurements. The regions underneath the ohmic contacts were modeled as heavily doped regions to give way to an ohmic behavior.

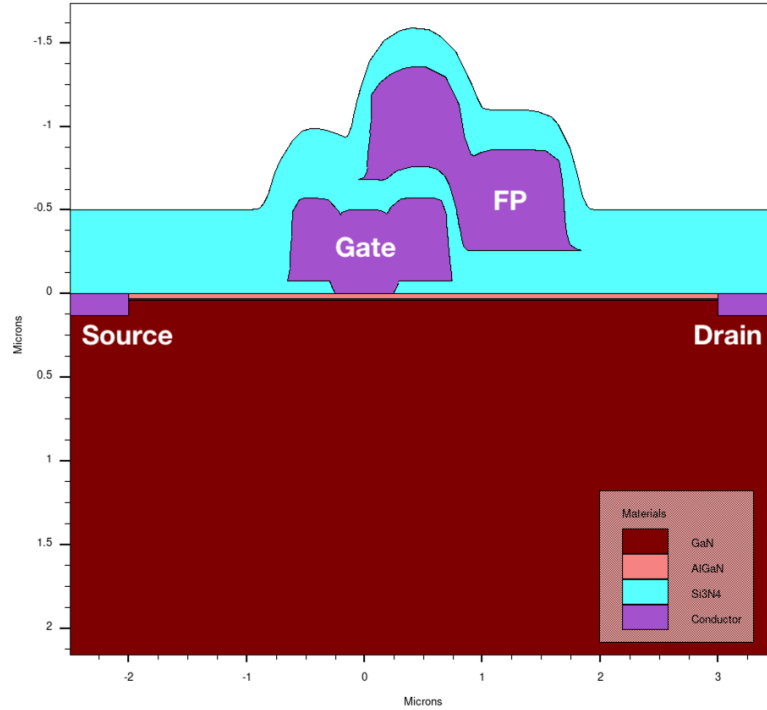


Figure 2.2: Simulation model of a GaN HEMT constructed using the ATHENA software.

2.1.2 Buffer Traps

Although often overlooked or understated in current literature, accurately modeling the electrical characteristics of buffer traps is an essential component of the GaN HEMT simulations. Buffer traps significantly contribute to current dispersion effects. Moreover, they lead to parasitic behaviors such as short-channel effects. Therefore, a precise assessment of buffer traps is a critical factor in ensuring the accuracy of the simulations. In this section, we focus on three major types of electron traps: nitrogen vacancies, carbon, and iron. While iron is intentionally introduced into the wafer during the growth [13], nitrogen vacancies and carbon are unfortunate byproducts of the growth processes [14].

N-type autodoping continues to be a pervasive issue in GaN growth, which makes device fabrication on undoped substrates impractical. To mitigate the impact of leaky behavior on device performance and eliminate the n-type conductive behavior, it has been commonly accepted in the literature to introduce Fe dopants during epitaxial

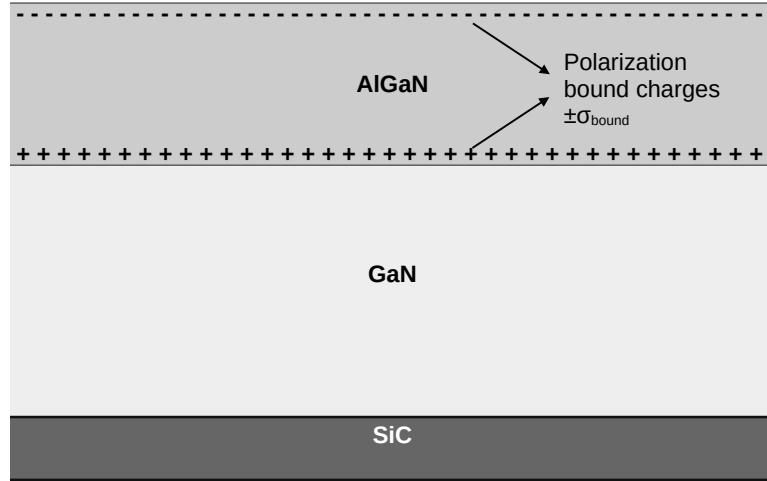


Figure 2.3: Two-dimensional schematic depicting the placement of bound charges, critical to the formation of the 2DEG.

growth. A typical Fe profile is given in Figure 2.4. While iron doping reduces substrate leakage and prevents parasitic conduction channels from forming away from the actual channel, traps associated with iron dopants (referred to as E2 in the literature) can either cause or exacerbate dispersion effects [14]. As such, the Fe source is stopped at around 1.1 micrometer thickness during GaN growth, which results in the peculiar exponential decay of the Fe concentration shown in Figure 2.4. Additionally, the carbon concentration is controlled by varying the growth conditions of individual layers. As such, the channel-GaN, as illustrated in Figure 2.4, exhibits a lower concentration of carbon compared to the transition and Fe-doped regions.

It has been postulated that the n-type behavior of GaN substrates originates from the presence of carbon contaminants [15]. However, as demonstrated by secondary-ion mass spectroscopy (SIMS), carbon concentrations are relatively low (Figure 2.4), and therefore another explanation was required. It was proposed that the n-type behavior could be attributed to nitrogen vacancies [16]. Several numerical studies have shown that nitrogen is a donor-type electron trap situated at the conduction band edge, thereby resulting in all donors being ionized [17]. In this study, we will also show that carbon densities are too low to account for some of the observed parasitic phenomena.

First, we start with the trap modeling. The influence of traps were considered as a

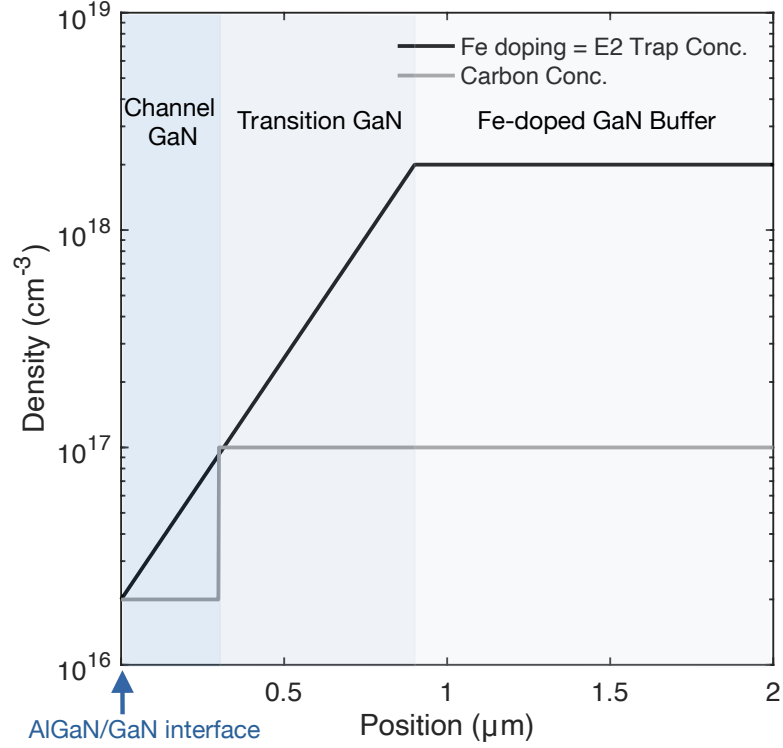


Figure 2.4: Plot illustrating the distribution of doping and impurity concentrations.

recombination-generation problem, wherein the net generation can be expressed as

$$U_{SRH} = \frac{pn - n_i^2}{\tau_p \left[n + n_i \exp\left(\frac{E_t - E_i}{kT}\right) \right] + \tau_n \left[p + n_i \exp\left(\frac{E_i - E_t}{kT}\right) \right]}, \quad (2.1)$$

where p , n , and n_i are the hole, electron, and intrinsic carrier densities, $\tau_{p,n}$ are trap lifetimes, $E_t - E_i$ is the trap energy in alignment with the intrinsic Fermi level, k is Boltzmann constant, and T is temperature [18]. The net generation U_{SRH} constitutes the right-hand-side of the carrier continuity equations as follows:

$$\frac{\nabla \cdot \mathbf{J}_n}{q} = U_{SRH}. \quad (2.2)$$

Next, the alignment of trap energies within the forbidden gap is discussed. Despite the significant scatter reported energy values show, iron related traps are very well established to be deep acceptors, and numerous sources locate them 0.6 eV below the conduction band edge [13]. While modeling the impact of iron is straightforward, the behavior of carbon contaminants is still open to discussion. However, recent reports posit that carbon functions as an amphoteric trap, with a significant proportion of acceptor traps being compensated by the donor portion. The energy values associated

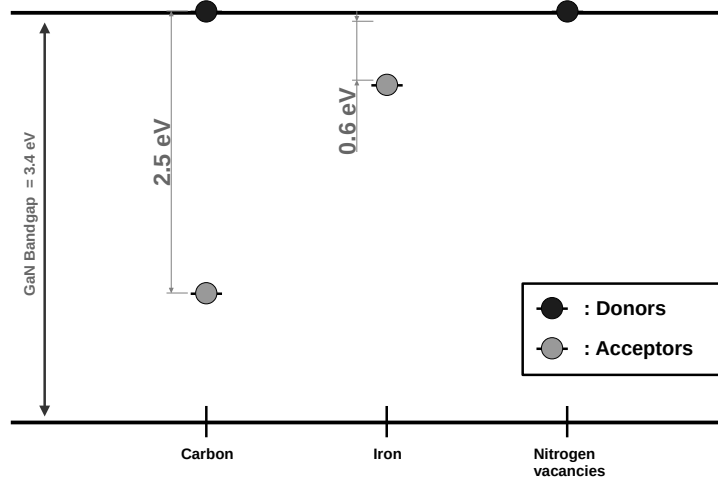


Figure 2.5: Graphic representation of the energy levels associated with impurities and point defects.

with carbon were taken from reference [13]. The energy values are outlined in Figure 2.5.

The compensation ratio of acceptors by donors can be expressed as follows:

$$\text{Compensation ratio} = \frac{\text{Total carbon conc.}}{\text{Acceptor carbon traps}} - 1, \quad (2.3)$$

where

$$\text{Total carbon conc.} = \text{Acceptor carbon traps} + \text{Donor carbon traps}. \quad (2.4)$$

In the modeling, the compensation ratio was taken to be 0.6, and the nitrogen vacancy concentration was assumed to be $3 \times 10^{16} \text{ cm}^{-3}$, to give way to n-type insulating behavior in the substrate. The resultant band diagram of a typical AlGaIn/GaN heterojunction is illustrated in Figure 2.6, as calculated using Silvaco ATLAS. As shown, the incorporation of traps render the GaN buffer an insulating n-type substrate, in alignment with the behavior typically observed in commercial wafers. It should be noted that the Fermi level is almost pinned at the iron level ($E_c - 0.6 \text{ eV}$).

Finally, the implications of trap modeling are discussed in the context of breakdown modeling. To showcase the function of traps in modeling, a parasitic behavior was studied by setting the drain voltage to 150 V while the gate voltage was -8 V. This

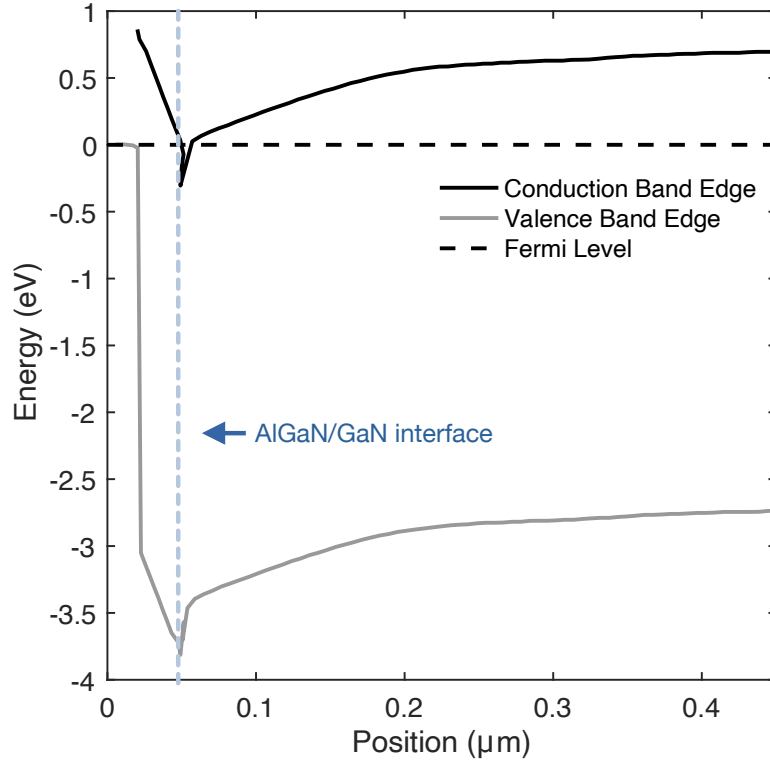


Figure 2.6: Band diagram of the simulated AlGaN/GaN heterojunction.

represents a typical breakdown measurement scenario, wherein devices are evaluated for their ability to inhibit current flow. Figure 2.7 displays the current density simulation results. It should be noted that at this bias point, the simulation model predicts an almost 1 mA/mm current density, which is in alignment with experimental observations [19, 20]. As shown in the figure, while the large negative voltage of the gate electrode depletes the channel in the vicinity of the barrier, it has minimal influence over the parasitic conduction paths deep within the buffer layer. This also shows that, despite the almost 3 micrometers long gate-to-drain region, the drain electrode does still exert significant influence over the conductivity of the channel, thereby giving rise to an effect commonly referred to as drain-induced barrier lowering [21].

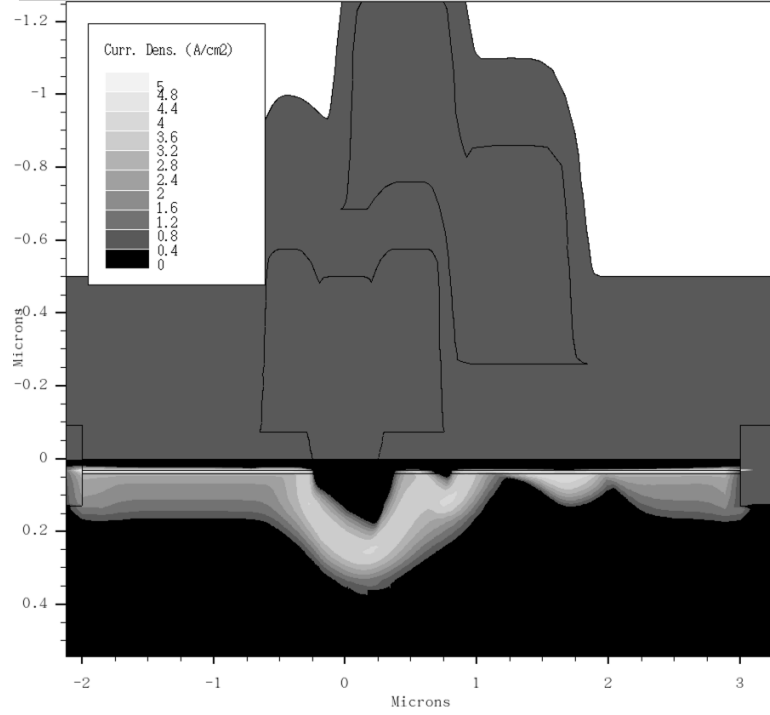


Figure 2.7: Breakdown simulation results depicting the current density and the onset of punch-through phenomenon.

2.1.3 Density-dependent Electron Mobility Model Development

Mobility modeling is a fundamental aspect of semiconductor device simulations. Electron mobility governs not only the current densities, but also the high-frequency performance, electron transit delay, and electric field distribution. Therefore, it is critical that the mobility model accurately reflects the underlying device physics. The conventional approach in the existing literature is to assume a mobility model of the form,

$$\mu_n(\mathcal{E}) = \mu_{n,0} \times \left\{ 1 + \left(\frac{\mu_{n,0}\mathcal{E}}{v_{\text{sat}}} \right)^\beta \right\}^{-\beta} \quad (2.5)$$

where \mathcal{E} is electric field, and adjust the parameters v_{sat} (saturation velocity), $\mu_{n,0}$ (low-field mobility), and β (a fitting parameter typically taken to be 1.5, which enables a smooth transition between the constant mobility and saturation regions) until the simulation results align with the measurements [22]. However, this method is time consuming, and often lacks precision due to its inherent simplicity.

Unlike many other semiconductors where electron velocity is constrained by mechanisms such as inter-valley electron transfer, it was found that the electron velocity in GaN is primarily limited by optical phonon scattering events, thereby rendering the saturation velocity electron density dependent. Bajaj *et al.* have studied this dependence extensively, and discovered that the relationship can be captured by a rational equation of the following form

$$v_{\text{sat}}(n_s) = \frac{10^7 \text{ cm/s}}{0.38 + \left(\frac{n_s}{n_{s,0}}\right)^{0.45}}, \quad (2.6)$$

where $n_{s,0}$ is $1.8 \times 10^{13} \text{ cm}^{-2}$ [23].

In this section, we propose a density-dependent electron mobility model based on the equation developed by Bajaj [23]. Furthermore, we outline a comprehensive calibration methodology that has been formulated around this mobility model.

2.1.3.1 Implementation

The calibration methodology development starts with the implementation of the mobility model. Conventional simulation programs typically treat charge transport as a drift-diffusion problem. Ignoring the diffusion components, the current density can be written as

$$\mathbf{J}_n \approx -qv_n n, \quad (2.7)$$

where \mathbf{J}_n is the current density (A/cm^2), q is the elementary charge, v_n is the electron velocity, and n is the electron density [18]. The electron velocity v_n is

$$v_n = \mathcal{E} \times \mu_n(\mathcal{E}). \quad (2.8)$$

To take the density dependence into account, we combine equations 2.5 and 2.6 as follows:

$$\mu_n(\mathcal{E}) = \mu_{n,0} \times \left\{ 1 + \left(\frac{\mu_{n,0} \mathcal{E}}{\frac{10^7 \text{ cm/s}}{0.38 + \left(\frac{n_s}{n_{s,0}}\right)^{0.45}}} \right)^\beta \right\}^{-\beta} \quad (2.9)$$

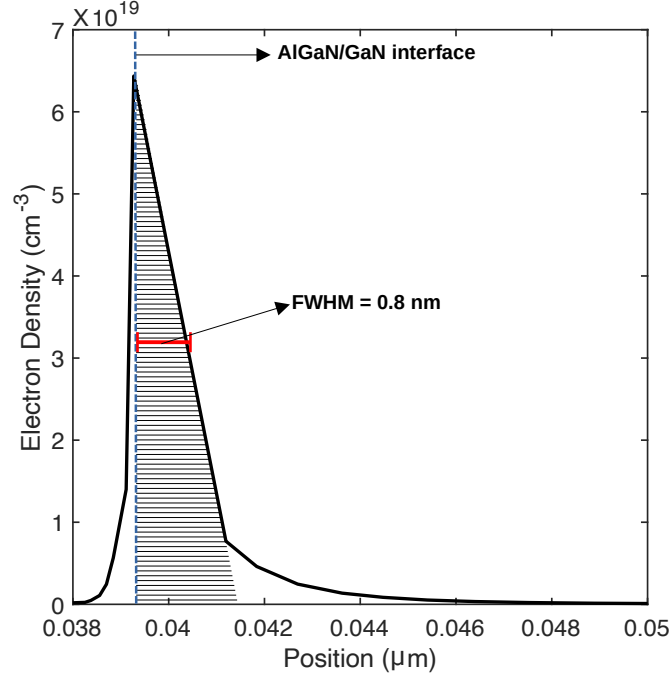


Figure 2.8: Distribution of 2DEG density without considering the quantization effects on the density of states.

The charge transport model used in this work is local in nature, in that it does not account for long-range interactions among carriers. In other words, the simulation model does not recognize the sheet charge density n_s . Therefore, in its full form, equation 2.9 is unusable in a simulation program. Hence, we need to convert the sheet charge density to volumetric density in order to input the mobility model into the simulation. We can accomplish this by making a simplifying assumption. As shown in Figure 2.8, the electron density in the channel of a typical GaN HEMT assumes a triangular distribution. Therefore, given the peak density at any point, we can determine a corresponding sheet charge density n_s by considering the full-width half maximum (FWHM) of the distribution as follows:

$$\begin{aligned}
 n_s &= \frac{2 \times n \times \text{FWHM}}{2} \\
 &= n \times \text{FWHM}.
 \end{aligned} \tag{2.10}$$

With this, the mobility equation becomes

$$\mu_n(\mathcal{E}, n) = \mu_{n,0} \times \left\{ 1 + \left(\frac{\mu_{n,0} \times \mathcal{E}}{10^7 \text{ cm/s}} \times \left[0.38 + \left(\frac{n \times \text{FWHM}}{n_{s,0}} \right)^{0.45} \right] \right)^\beta \right\}^{-\beta}. \tag{2.11}$$

Table 2.1: Explanation and details of the proposed calibration procedure.

Step	Procedure
1	Configure the geometry of the transistor model to accurately reflect the actual dimensions of the device.
2	Ensure the 2DEG density in the simulation matches the measured values. This should be accomplished by adjusting the bound charge density σ_{bound} .
3	Configure the low-field mobility value to align with the Hall mobility value as obtained from measurements.
4	Configure the resistance of the ohmic contacts in the simulation model to align with the experimentally reported values.
5	Finally, modify the work function of the gate electrode to adjust the threshold voltage of the simulation model until it aligns with the observed data.

Table 2.2: Transistor geometry, reported results, and simulation model outputs.

Process Details				
L_G	L_{SD}	f_T	f_T using the calibrated model	Ref
140 nm	1 μm	97 GHz	100 GHz	[24]
250 nm	2 μm	67 GHz	73 GHz	[25]

2.1.3.2 Calibration Procedure and Verification of the Model

The calibration procedure is outlined in Table 2.1. As shown, the calibration procedure entails configuring the simulation variables to match measured transistor parameters such as the 2DEG density and transistor geometry. To showcase the capabilities, versatility, and universality of the proposed procedure, the model was validated using actual measurements reported in the existing literature. First, the transfer characteristics were investigated. As displayed in Figure 2.9, the simulation model shows an excellent agreement with the measurements. Next, the high-frequency characteristics of the simulation model were investigated by calculating the current-gain cut-off frequencies of the models. Small signal characteristics also show a close match to the measurements, thus showcasing the model’s ability to accurately capture electron transport dynamics. These results are summarized in Table 2.2.

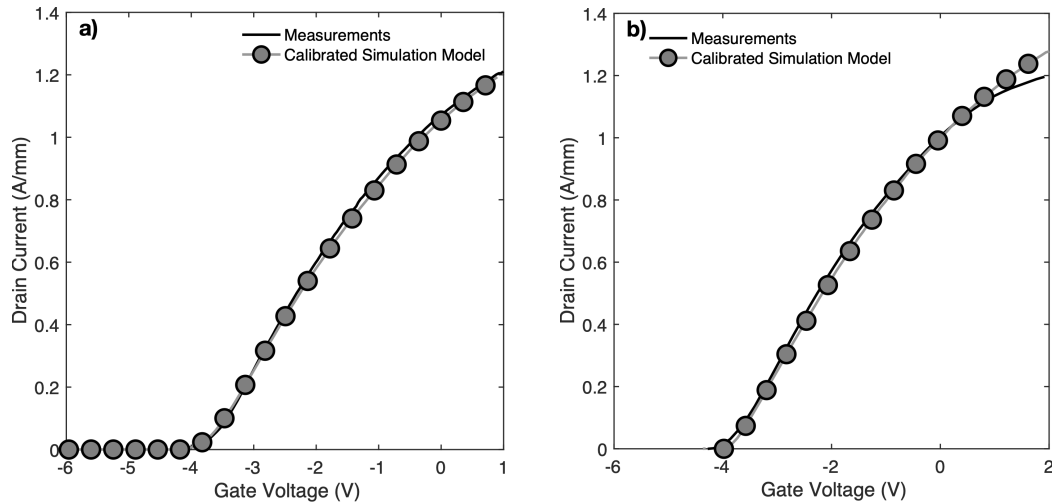


Figure 2.9: Calibration results compared to the measurement data reported in References 24 (a) and 25 (b).

2.2 Solid-mechanics Simulations

Mechanical stresses play a critical role in the performance and reliability of GaN HEMTs. Understanding the interplay between mechanical stresses and electrical properties is crucial for optimizing device performance. Mechanical simulations serve as an essential tool for this purpose, as they allow for the prediction and analysis of stress distributions within the material. Through mechanical simulations, we can gain insights into how stresses and strains in the material affect the electrical properties of GaN HEMTs. In addition, gaining a clear understanding of the stress distributions within the epitaxy could serve as a guide to identify potential sites for defect generation. In this section, we will focus on the methodologies employed in solid-mechanics simulations. Specifically, we will introduce the equations that are central to the simulations and discuss the proper choice and calculation of material properties that are vital for accurate modeling.

2.2.1 Overview of the Simulation Model

Stresses and strains were analyzed under the assumption of linear elasticity using COMSOL's Structural Mechanics module [26]. The governing equation of the linear

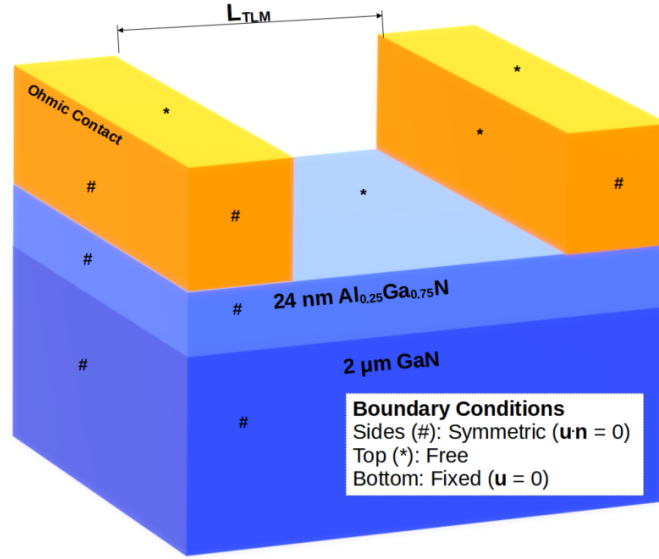


Figure 2.10: Three-dimensional simulation model. Boundary conditions associated with surfaces are displayed with symbols.

elasticity simulations was the static equilibrium equation

$$\nabla \cdot \boldsymbol{\sigma} = 0, \quad (2.12)$$

where $\boldsymbol{\sigma}$ is the Cauchy stress tensor. The static equilibrium equation was subject to Hooke's law for linear elastic materials

$$\boldsymbol{\sigma} = \boldsymbol{\sigma}_{\text{ext}} + \boldsymbol{C} : (\boldsymbol{\varepsilon} - \boldsymbol{\varepsilon}_{\text{ext}}), \quad (2.13)$$

where \boldsymbol{C} is the material stiffness tensor, $\boldsymbol{\sigma}_{\text{ext}}$ and $\boldsymbol{\varepsilon}_{\text{ext}}$ are the external stresses and strains which may optionally be defined for a particular region of the geometry to model residual, ohmic, and lattice mismatch strains or stresses, and $\boldsymbol{\varepsilon}$ is the strain tensor. The ":" operator defines a summation over two indices as follows:

$$\sigma_{ij} = \sum_{k=1}^3 \sum_{l=1}^3 C_{ijkl} \varepsilon_{kl} \quad (2.14)$$

The equilibrium equation and Hooke's law were solved under the premise of infinitesimal strains

$$\boldsymbol{\varepsilon} = \frac{1}{2} [\nabla \boldsymbol{u} + (\nabla \boldsymbol{u})^T], \quad (2.15)$$

where \boldsymbol{u} is the mechanical displacement vector.

Table 2.3: Elastic properties of the anisotropic simulation materials.

		GaN	AlN	Al _{0.25} Ga _{0.75} N
C_{11}		367	396	374.25
C_{12}		135	137	135.50
C_{13}	GPa	103	108	104.25
C_{33}		405	373	397.00
C_{44}		95	116	100.25

Table 2.4: Elastic properties of the ohmic contact simulation material. Young's Modulus of the ohmic contact material was calculated from the material constants of Ti, Al, Ni, and Au.

		Ti	Al	Ni	Au	Ohmic Contact
E	GPa	115.7	70.0	219.0	70.0	107.7
ν	-	0.32	0.35	0.31	0.44	0.3

The three-dimensional simulation geometry is displayed in Figure 2.10. The simulation geometry was configured to reflect the actual device dimensions. As measured by the wafer curvature method, the silicon nitride layers deposited on silicon substrates exhibited stresses below 100 MPa. Therefore, the silicon nitride passivation layer was not modeled. The bottom of the GaN was configured as a fixed boundary ($u = 0$). The sides were set as symmetric planes, while the top surfaces were configured to be free boundaries.

Properties of the anisotropic materials used in the simulation model are listed in Table 2.3 [27, 28]. GaN and Al_{0.25}Ga_{0.75}N were modeled as anisotropic materials. Elastic properties of the Al_{0.25}Ga_{0.75}N barrier were calculated using linear interpolation. Ohmic contacts were modeled as isotropic materials. The Young's Modulus of the ohmic contact material was calculated by assuming the validity of the rule of mixtures principle for quaternary alloys, i.e.,

$$E_{\text{ohmic}} = \frac{1}{\text{Total Ohmic Contact Volume}} \sum_{i = \text{Ti, Al, Ni, Au}} V_i E_i, \quad (2.16)$$

where V_i is the volume and E_i is the Young's Modulus of the i th layer in the ohmic stack [29]. The Poisson ratio ν of the ohmic contact material was assumed to be 0.3 as most metals have a ν of about 0.3. Properties of the ohmic contact material, Ti, Al, Ni, and Au are summarized in Table 2.4. These values were retrieved from the COMSOL

Table 2.5: Stress-free lattice parameters used in the calculation of the barrier strain.

Material		a
GaN		3.18780
AlN	Å	3.11197
AlGaIn		3.16880

material library [26].

2.2.2 Stress Definitions

Stresses in the AlGaIn barrier, GaN substrate, and ohmic contact metals were considered in the simulations. The exact values of these stresses are discussed in later chapters as they were determined in light of the Raman measurement results to reproduce the experimental data in the simulations. The ohmic contacts were assumed to be under isotropic tensile stress, i.e.,

$$\sigma_{\text{ext, ohmic}} = \begin{bmatrix} \sigma_{\text{ohmic}} & 0 & 0 \\ 0 & \sigma_{\text{ohmic}} & 0 \\ 0 & 0 & \sigma_{\text{ohmic}} \end{bmatrix}. \quad (2.17)$$

The substrate residual stress was assumed to be purely biaxial and homogenous [30, 31]. Therefore, in the GaN layer, the external stress was set as

$$\sigma_{\text{ext, GaN}} = \begin{bmatrix} \sigma_{\text{res}} & 0 & 0 \\ 0 & \sigma_{\text{res}} & 0 \\ 0 & 0 & 0 \end{bmatrix}. \quad (2.18)$$

The pseudomorphically grown fully-strained barrier layer assumes the a-axis lattice constant of the GaN substrate in the heterojunction plane, i.e., $a_{\text{GaIn}} = a_{\text{AlGaIn}}$ [31]. If the stress in the GaN substrate is known and can be assumed to be uniform, the GaN lattice constant can be calculated from the in-plane strain. Generally, the stress in the substrate is heterogeneous due to the patterns on the top surface and the varying growth conditions of different layers during the MOCVD growth. However, to simplify the treatment, we assumed that stresses in the substrate are uniform and are equal to the residual stress σ_{res} . The residual stress can be associated with the in-plane strain of the

GaN layer as follows:

$$\begin{aligned}\sigma_{\text{res}} &= Y \varepsilon_{a, \text{GaN}} \\ &= \underbrace{(C_{11} + C_{12} - 2C_{13}^2/C_{33})}_Y \times \underbrace{\frac{a_{\text{GaN}} - a_{\text{relaxed, GaN}}}{a_{\text{relaxed, GaN}}}}_{\varepsilon_{a, \text{GaN}}},\end{aligned}\quad (2.19)$$

where $a_{\text{relaxed, GaN}}$ is the stress-free a-axis lattice constant of GaN [31]. Rewriting equation 2.19 and asserting $a_{\text{GaN}} = a_{\text{AlGaN}}$, the barrier lattice constant a_{AlGaN} is

$$a_{\text{AlGaN}} = a_{\text{relaxed, GaN}} \left(\frac{\sigma_{\text{res}}}{Y} + 1 \right). \quad (2.20)$$

Then, the in-plane strain $\varepsilon_{a, \text{AlGaN}}$ in the barrier layer can be calculated from the lattice constant of the barrier, i.e.,

$$\varepsilon_{a, \text{AlGaN}} = \frac{a_{\text{AlGaN}} - a_{\text{relaxed, AlGaN}}}{a_{\text{relaxed, AlGaN}}}, \quad (2.21)$$

where $a_{\text{relaxed, AlGaN}}$ is the stress-free barrier lattice constant, which can be calculated by employing Vegard's law and using the relaxed GaN and AlN lattice parameters (Table 2.5) as follows

$$a_{\text{relaxed, AlGaN}} = x a_{\text{relaxed, AlN}} + (1 - x) a_{\text{relaxed, GaN}}, \quad (2.22)$$

where x is the Al concentration in the barrier. Given the in-plane barrier strain $\varepsilon_{a, \text{AlGaN}}$, the out-of-plane strain $\varepsilon_{c, \text{AlGaN}}$ can be calculated from the relation

$$\begin{aligned}\mathbf{R}^{\text{B}} &= -\frac{\varepsilon_{c, \text{AlGaN}}}{\varepsilon_{a, \text{AlGaN}}} \\ &= \frac{2C_{13}}{C_{33}}.\end{aligned}\quad (2.23)$$

In accordance with these equations, the external strain in the barrier was configured as follows:

$$\begin{aligned}\varepsilon_{\text{ext, AlGaN}} &= - \begin{bmatrix} \varepsilon_{a, \text{AlGaN}} & 0 & 0 \\ 0 & \varepsilon_{a, \text{AlGaN}} & 0 \\ 0 & 0 & \varepsilon_{c, \text{AlGaN}} \end{bmatrix} \\ &= - \begin{bmatrix} \varepsilon_{a, \text{AlGaN}} & 0 & 0 \\ 0 & \varepsilon_{a, \text{AlGaN}} & 0 \\ 0 & 0 & -\mathbf{R}^{\text{B}} \times \varepsilon_{a, \text{AlGaN}} \end{bmatrix}.\end{aligned}\quad (2.24)$$

2.3 Uncoupled Electro-mechanical Simulations

Electro-mechanical simulation studies assume a pivotal role in transistor research and development. Primarily, these studies enable us to exploit the interconnectedness of electrical and mechanical characteristics. For instance, in the CMOS industry, strains and stresses are regarded as design variables because they allow precise tuning of electron and hole mobility [32]. In the case of GaN based HEMTs, strain engineering provides a means to adjust both the two-dimensional electron gas density as well as electron saturation velocity. However, it is important to recognize that not all strain modifications have positive influences. For example, defects, which could either be inherently present in a crystal and/or generated during the fabrication or nominal operation, can also modify the strain. The strain fields emanating from these defects may adversely impact the transfer characteristics of transistors. Therefore, exploring these phenomena through electro-mechanical simulations can provide valuable insights into the mechanics of energy relaxation and electrical attributes of transistors, shaping our understanding of device reliability and performance. In the case of GaN HEMTs, the dominant link between electrical and mechanical characteristics is piezoelectricity. Therefore, as an initial step, the calculation methodology of polarization induced bound charge density at the AlGa_N/Ga_N interface is presented. Then, the simulation workflow is explained. Finally, as a case study, we turn our attention to FinHEMTs and explore the impact of fin width on channel conductivity.

2.3.1 Calculation of Polarization Induced Bound Charges

The bound charge density at the interface of AlGa_N/Ga_N heterojunction is given by the polarization field differences of the two media [10]. Note that this follows from Maxwell's laws and boundary conditions.

$$\sigma_{\text{bound}} = P_{\text{GaN}} - P_{\text{AlGaN}}. \quad (2.25)$$

For a Wurtzite crystal, the polarization field can be written as

$$P = P_{\text{SP}} + (\varepsilon_1 + \varepsilon_2)e_{31} + \varepsilon_3e_{33}, \quad (2.26)$$

where e_{3i} are the piezoelectricity constants, ε_i is the strain in the i th direction, and P_{SP} stands for the spontaneous polarization. If a material can be assumed to be under pure biaxial stress [31], the previous expression simplifies to

$$\begin{aligned} P &= P_{\text{SP}} + \underbrace{2\varepsilon_1}_{\varepsilon_1=\varepsilon_2} e_{31} - 2 \underbrace{\frac{C_{13}}{C_{33}}}_{\varepsilon_3=-2\frac{C_{13}}{C_{33}}} \varepsilon_1 e_{33} \\ &= P_{\text{SP}} + 2\varepsilon_1 \left(e_{31} - \frac{C_{13}}{C_{33}} e_{33} \right). \end{aligned} \quad (2.27)$$

In the case that the material is free of any mechanical strains, the last expression further simplifies to

$$P = P_{\text{SP}}. \quad (2.28)$$

Therefore, the bound charge density at the heterojunction interface can be given as

$$\sigma_{\text{bound}} = (P_{\text{SP, GaN}} - P_{\text{SP, AlGaIn}}) - 2\varepsilon_1 \left(e_{31} - \frac{C_{13}}{C_{33}} e_{33} \right). \quad (2.29)$$

2.3.2 Electro-mechanical Simulation Workflow

A typical uncoupled electro-mechanical simulation workflow involves the determination of strains in the barrier utilizing the methodology given in Section 2.2. Following this, a MATLAB program averages the strain data along the wafer growth direction. The resultant average strain is then used to calculate the bound charge density at the AlGaIn/GaN interface using ATLAS simulations as described in Section 2.1. It should be emphasized that the simulations are uncoupled, indicating that while mechanical properties inform the electrical charge densities, the electrical properties do not reciprocally impact the mechanical properties. This is a simplification, yet a necessary one, enabling computationally feasible simulations.

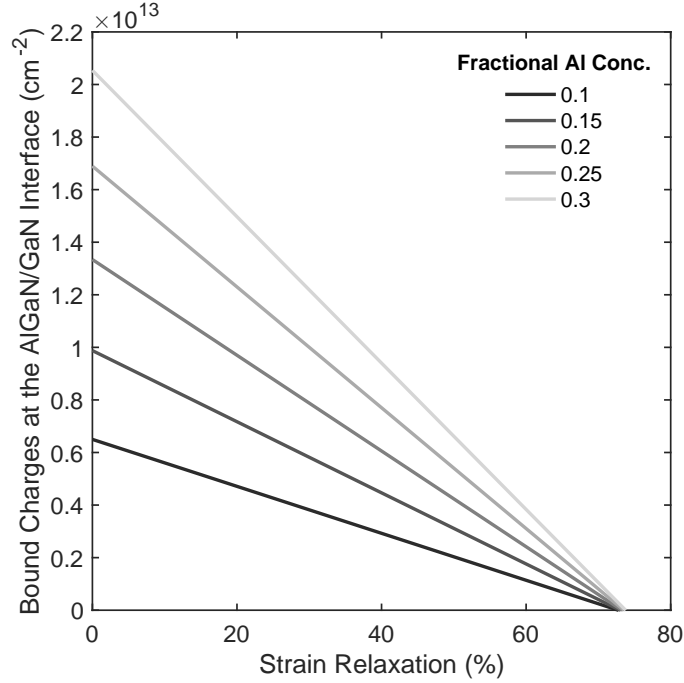


Figure 2.11: Illustration of the impact of strain relaxation on bound charge density.

First, we start with the bound charge density at the AlGaIn/GaN interface with respect to the strain relaxation percentage. This is depicted in Figure 2.11. Unlike the commonly employed polarization coefficients given in reference [2], this recently introduced polarization field calculation method anticipates a much more rapid decrease of the 2DEG density [10]. This highlights the paramount importance of an accurate representation of polarization charges, particularly when examining the impact of strain relaxations induced by defect generations and fin formations.

2.3.3 Case Study

Next, we discuss the impact of fin formation on 2DEG density distribution and channel conductivity. FinHEMTs have recently gained popularity due to their ability to provide enhanced linearity [33]. Central to this enhancement is the reduction of the peak 2DEG density, thereby enabling fast optical phonon removal, which in turn enhances the saturation velocity of the carriers. A detailed discussion on these subjects can be

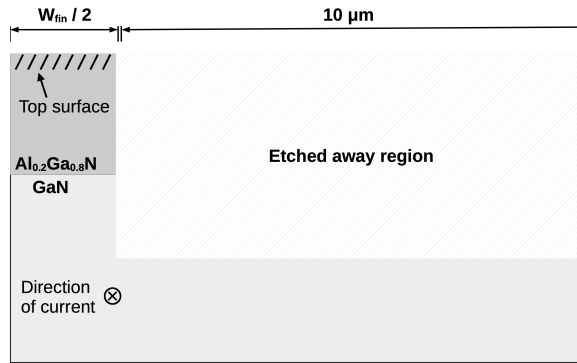


Figure 2.12: Two-dimensional depiction of the fin simulation model analyzed using COMSOL simulations.

found in references [34, 35, 36]. COMSOL simulation settings of a typical fin structure are given in Figure 2.12. In this structure, electrical current flow is confined to the fins. Moreover, it is assumed that the areas beneath the etched away regions are fully insulating. This is due to the fact that with the removal of the barrier, the source of the 2DEG - the piezoelectricity differences between the barrier and buffer - is effectively eliminated. Strains, stresses, and boundary conditions follow from the previous section. In contrast to the previous section, however, the case of the fixed top boundary condition was also studied. This was an attempt at emulating the influence of gate metal, which could mechanically reinforce the fins and thereby reduce the deformation and relaxation.

Figure 2.13 illustrates the barrier strain distributions and Figure 2.14 shows the mean barrier strains in response to changing fin width as calculated using the COMSOL model. Under both boundary condition cases, the mean strain of the barrier, which is the source of 2DEG in the channel, exhibits a rapid loss with decreasing fin width. The fin formation action creates new surfaces, upon which the coherently strained barrier can alleviate its accumulated elastic energy through the deformation of the said surfaces. Bound charge densities were then studied using ATLAS simulations to reveal the 2DEG distributions in the channel. Figure 2.15 displays the distributions, while Figure 2.16 presents the average 2DEG density across the channel of a fin. As indicated in Figure 2.15, fin formation presents a unique opportunity to engineer the 2DEG densities. This, in turn, allows for the fine-tuning and/or improvement of the threshold voltage, device linearity, and even device reliability.

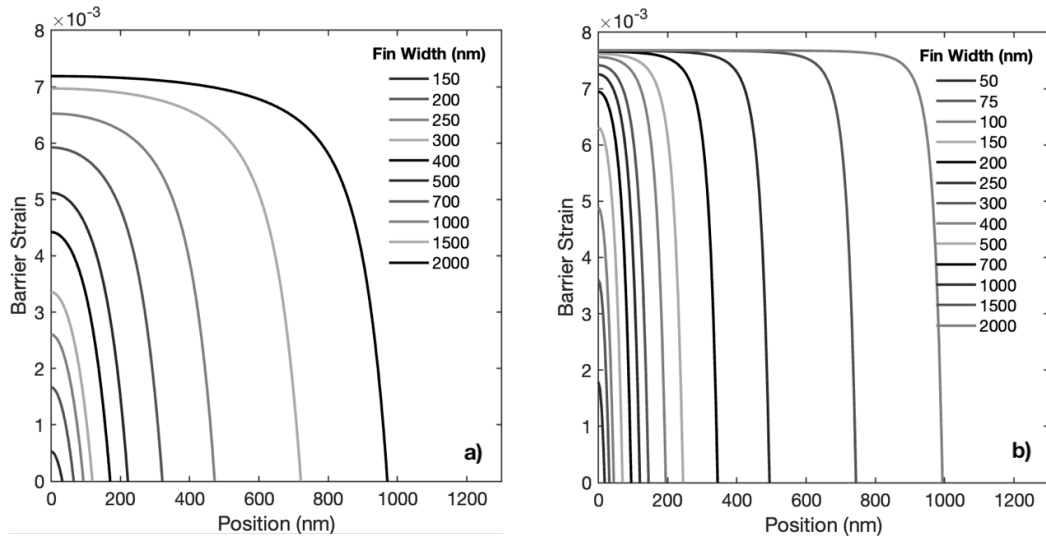


Figure 2.13: Distribution of barrier strain in relation to fin width. Two boundary condition cases were studied. a) shows the results from the free top surface boundary condition case, whereas b) illustrates the impact of a fixed top surface boundary condition.

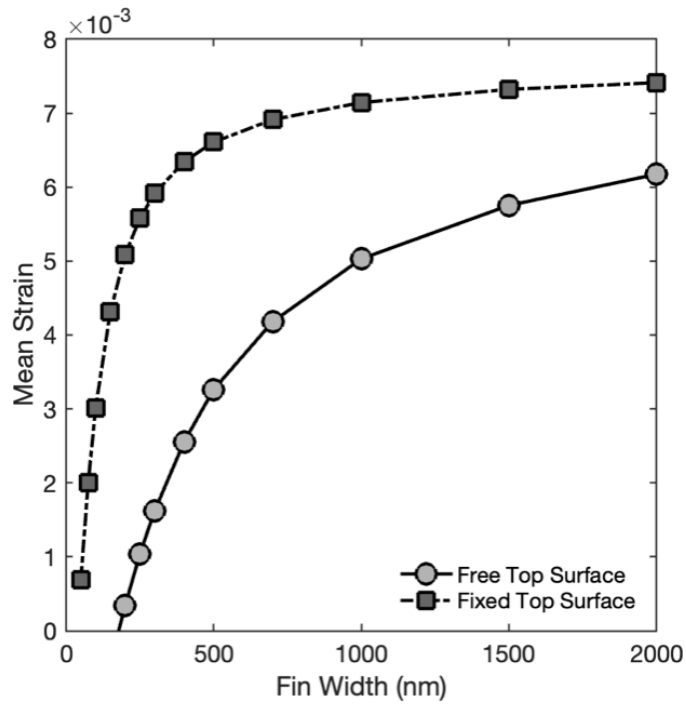


Figure 2.14: Average strain as a function of fin width.

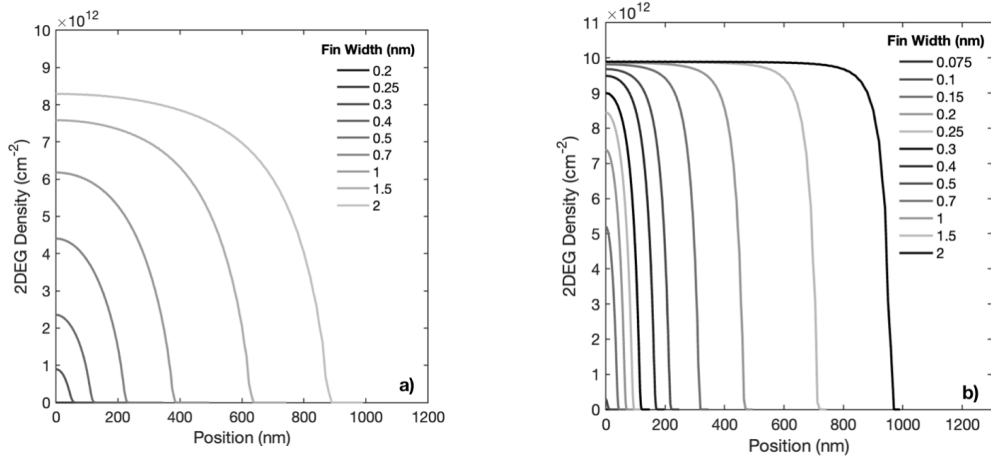


Figure 2.15: Variation of 2DEG distribution with respect to fin width. Two boundary condition cases were studied. a) shows the results from the free top surface boundary condition case, whereas b) illustrates the impact of a fixed top surface boundary condition. Strain distribution results displayed in Figure 2.13 were converted to polarization charges by following the workflow explained in Section 2.3.1. Then, ATLAS calculated the resulting 2DEG densities and distributions.

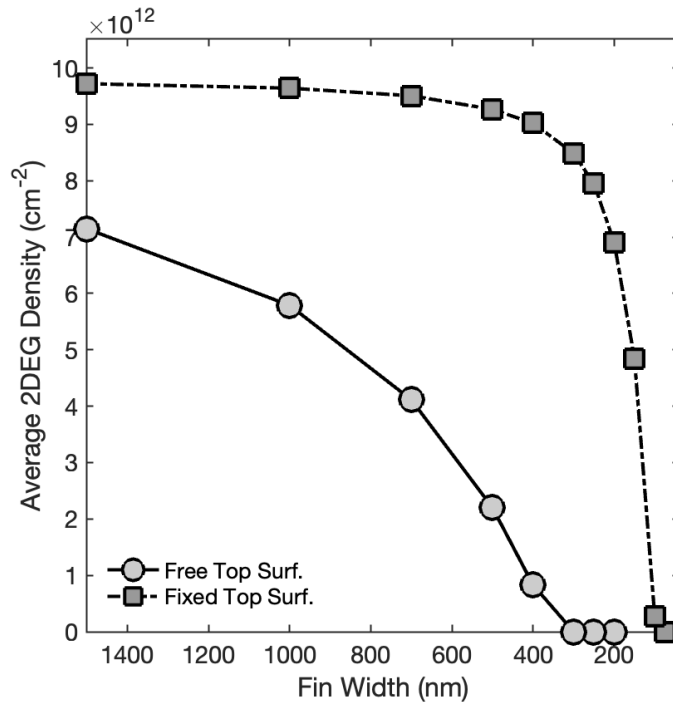


Figure 2.16: Average 2DEG density as a function of fin width.

Chapter 3

Analysis and Modeling of Mechanical Stresses in Ungated AlGa_N/Ga_N HEMTs using μ Raman Spectroscopy

3.1 Motivation

GaN-based high electron mobility transistors (HEMTs) have attracted considerable attention due to their large breakdown voltages, high cut-off frequencies, and low sheet resistances. These attributes make GaN HEMTs and GaN power amplifiers excellent candidates for use in radars, 5G base stations, and satellite communications. Despite the significant advancements in the device performance, the degradation dynamics are still not well understood [37]. Commonly reported driving forces of device failure during the nominal operation of HEMTs are poor crystal quality, electric fields, leakage currents, and hot carrier effects [38, 39, 40, 41]. Degradation during device fabrication continues to be a significant concern, and it's commonly attributed to high-temperature processes such as ohmic anneals, as well as plasma damage and thin film depositions [42].

Mechanical stresses accelerate device degradation during nominal operation and

fabrication. For instance, pit formation is commonly observed with off-state stressing, which is attributed to the inherent link between electric fields and mechanical stresses. Pits tend to occur under the drain edge of the gate electrode, where electric fields concentrate during electrical stressing [41]. These electric fields elevate the barrier's elastic energy via the inverse piezoelectric effect (IPE). In response, the AlGaN barrier relaxes the increased elastic energy by generating defects, thereby enabling pit formation [39]. Such defects can deteriorate the device performance and reduce the operating lifetime. Therefore, the accurate modeling and quantification of mechanical stresses are highly desired from a device engineering perspective.

Mechanical stresses can be accurately measured using Raman spectroscopy. Raman spectroscopy is a noninvasive characterization technique that measures the frequencies of phonon modes, many of which are highly sensitive to stress [43]. The major drawback of Raman spectroscopy is its low spatial resolution (≈ 1 micrometer), even in the confocal mode. GaN devices are typically 3-5 micrometers long. With micrometer size resolution, only several stress measurements can be acquired along the length of the device. Therefore, Raman spectroscopy should be combined with simulations for high-fidelity evaluation of mechanical stresses.

Therefore, this work first attempted to establish a link between mechanical simulations with Raman measurements. A simulation calibration procedure was proposed. Raman measurements taken from the center of ungated HEMTs were used to calibrate the mechanical model. Stress and elastic energy distributions obtained from the calibrated model were then utilized to pinpoint potential sites for defect generation. The model's findings were compared with experimentally observed defect generation behavior documented in the literature. Finally, the implications of defect generation on ohmic contact resistance and overall device performance were analyzed and discussed.

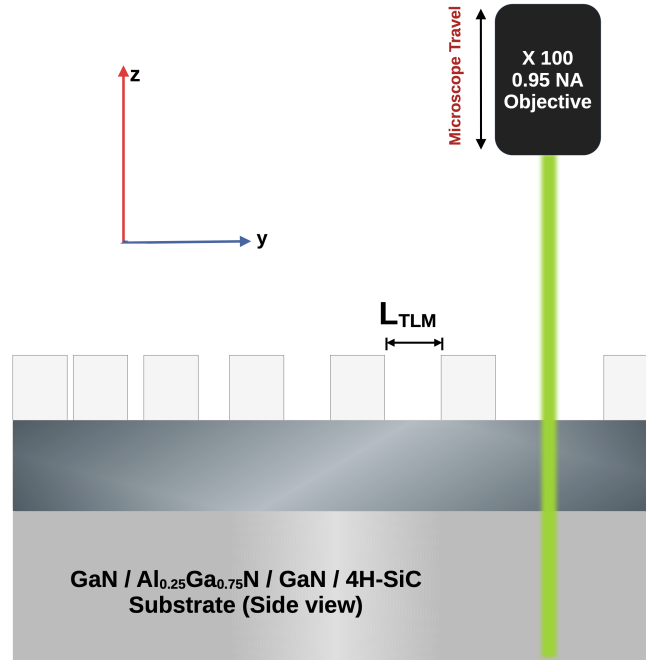


Figure 3.1: Cross-sectional view of the devices. The laser beam was focused onto the center of two ohmic contacts. The fine focus was accomplished by adjusting the z-axis position of the microscope objective.

3.2 Experimental Methodology

3.2.1 Ungated HEMTs

The GaN (3 nm) / Al_{0.25}Ga_{0.75}N (24 nm) / GaN (2 μm) epitaxial structure was grown on a 3" 4H-SiC substrate by metal-organic chemical vapor deposition. Ungated HEMT devices of varying drain-to-source spacings L_{DS} were fabricated in close proximity. Fabrication was commenced with the ohmic contact patterning by optical lithography. Then, a Ti (12 nm) / Al (100 nm) / Ni (50 nm) / Au (50 nm) stack was deposited via electron beam evaporation. Ohmic contacts were annealed in an N₂ environment at 840° C for 30 s. Inter-device isolation was accomplished by a 500 nm deep etching by a Cl₂-based inductively coupled plasma-reactive ion process. A 75 nm silicon nitride passivation layer was deposited in a plasma-enhanced chemical-vapor-deposition system. Figure 3.1 shows the cross-section view of the devices.

3.2.2 μ Raman Spectroscopy

3.2.2.1 Measurement Configuration

μ Raman spectroscopy was used to measure the stress in the ungated HEMTs. Measurements were performed at room temperature using a WITec alpha confocal Raman microscope. The laser beam ($\lambda = 532$ nm) was delivered on the (0001) surface. Unpolarized Raman spectra were collected in the backscattering geometry, i.e., detection and excitation were carried out through the same objective lens (0.95 NA). The spectrometer's charge-coupled device (CCD) was cooled down to -60° C. CCD was operated in the full vertical binning mode to enhance the signal-to-noise ratio (SNR). Vertical and horizontal shifting speeds of the CCD were $8.25 \mu\text{s}$ and 33 kHz, respectively. CCD's spectral center was set to 526 cm^{-1} . An 1800 grooves/mm grating enabled a spectral resolution of about 1.19 cm^{-1} near the GaN E_2 (high) signal. A mercury plasma transition line ($^3\text{P}^\circ$) situated at 546.075 nm was used to calibrate the spectrometer [44].

The beam must be tightly focused to enhance the SNR, improve the repeatability and stray light rejection, and minimize the measurement duration. Minimizing the measurement duration has several benefits. Notably, shorter measurements are less susceptible to temperature drifts and random errors. Therefore, to find the optimal lens position that maximized the GaN E_2 signal, the microscope stage was traveled $10 \mu\text{m}$ along the c-axis with 100 nm steps. Raman spectra were collected at each step with a 1 s dwell period. Then, the spectra were integrated within the range $(550, 575) \text{ cm}^{-1}$. The integrated Raman results are given in Figure 3.2. Informed by these results, the objective stage was then set to the position which maximized the signal. Edge-spread measurements (Figure 3.3) were performed across a metal edge to calculate the beam size. The beam size was about 502 nm, which verified the tight focus.

3.2.2.2 Substrate Stress Calculation Procedure

Stress measurements were performed on the center of the ungated HEMT patterns, as shown in Figure 3.4. To reduce the influence of the morphological nonuniformities,

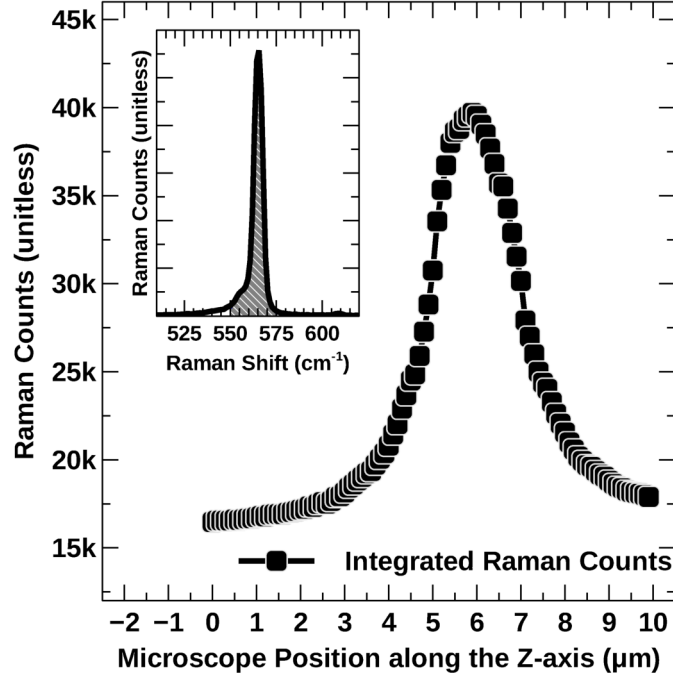


Figure 3.2: Integrated Raman counts were maximized for tight focus. Inset: Raman spectra were integrated within $(550, 575) \text{ cm}^{-1}$. The shaded area represents the integration range.

ten measurements were taken from points $1 \mu\text{m}$ apart. Dwell time per point was 10 s. Stress was measured by monitoring the peak position of the E_2 (high) mode. This choice was motivated by several factors. Compared to the A_1 mode, the E_2 mode is more sensitive to stress. Also, the E_2 mode's Raman scattering cross section is larger, resulting in larger SNR [43]. The peak position of the E_2 line was determined by deconvolving the normalized spectra within the range $(550, 575) \text{ cm}^{-1}$ into two Gaussian profiles. Figure 3.5 illustrates the deconvolution of the spectra into E_2 (high) and E_1 (TO) lines. In the backscattering configuration, E_1 (TO) mode is forbidden. However, the objective lens's high numerical aperture (0.95 NA) and disorder activation allowed the observation of the E_1 phonon line [43]. E_2 line peak positions and 99% confidence intervals (CI) as calculated using t-distribution are displayed in Figure 3.6.

The E_2 and A_1 modes exhibit a linear relation with the biaxial stress [30]. An increase (decrease) in the phonon frequency corresponds to a compressive (tensile) shift. This is expressed by

$$\Delta\omega_{\text{ph-mode}} = \omega - \omega_{0,\text{ph-mode}} = K_{\text{RS}}^{\text{ph-mode}} \sigma_a \quad (3.1)$$

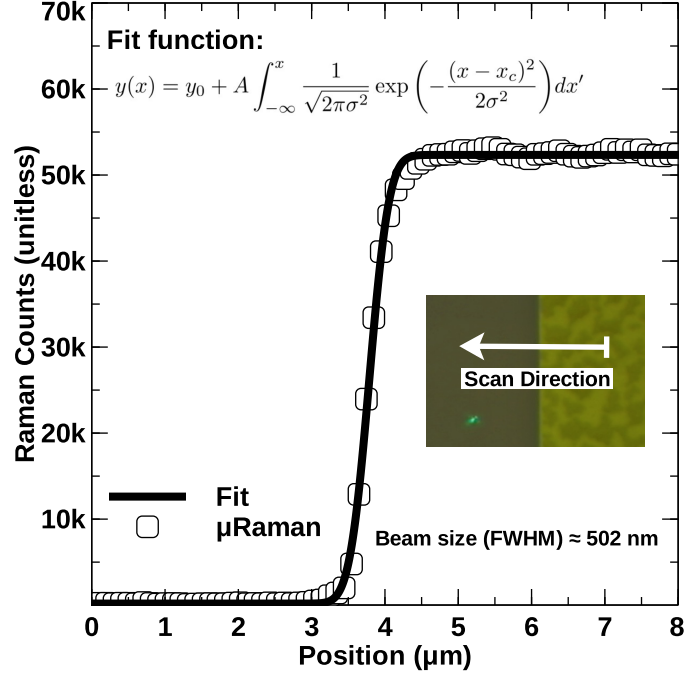


Figure 3.3: Knife-edge lateral resolution measurement results of the optical setup and Gaussian cumulative distribution function fit.

where $\Delta\omega_{\text{ph-mode}}$ is the difference between the measured phonon position (ω) and the stress-free reference frequency ($\omega_{0, \text{ph-mode}}$) in cm^{-1} , $K_{\text{RS}}^{\text{ph-mode}}$ is the constant that relates the frequency shifts to stress in $\text{cm}^{-1}/\text{GPa}$, and σ_a is the measured biaxial stress in GPa. The values of $\omega_{0, \text{ph-mode}}$ and K_{RS} were taken from Ref [30] and are listed in Table 3.1. Note that this relation only holds if the crystal is under pure biaxial stress [43]. The stress state can be determined by tracking the ratio of the peak frequency changes $\Delta_{A_1}/\Delta_{E_2}$ [45]. For the pure biaxial stress state, the $\Delta_{A_1}/\Delta_{E_2}$ ratio is given as $K_{\text{RS}}^{A_1}/K_{\text{RS}}^{E_2} \approx 0.69$ [30, 45]. To justify the use of the biaxial stress measurement relation,

Table 3.1: Proportionality constants and stress-free reference frequency used in the stress calculations.

		Phonon Modes	
		A_1 (TO)	E_2 (High)
$\omega_{0, \text{ph-mode}}$	cm^{-1}	733.94 ± 0.09	568.15 ± 0.13
$K_{\text{RS}}^{\text{ph-mode}}$	$\text{cm}^{-1}/\text{GPa}$		-3.09 ± 0.41

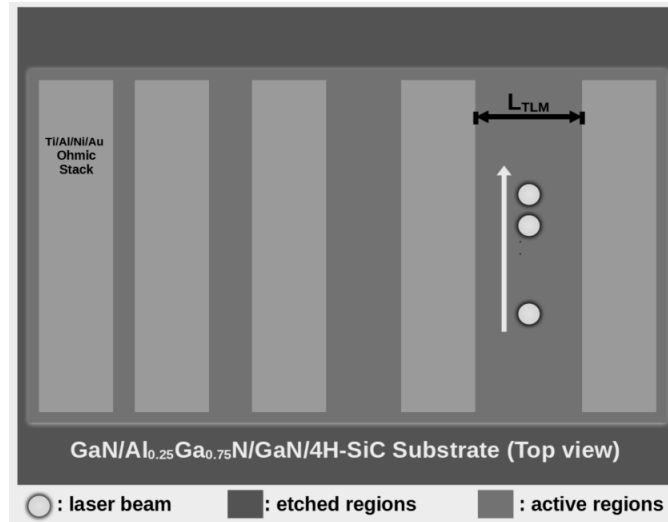


Figure 3.4: Top view of the devices. Ten consecutive measurements were taken from the center of the devices.

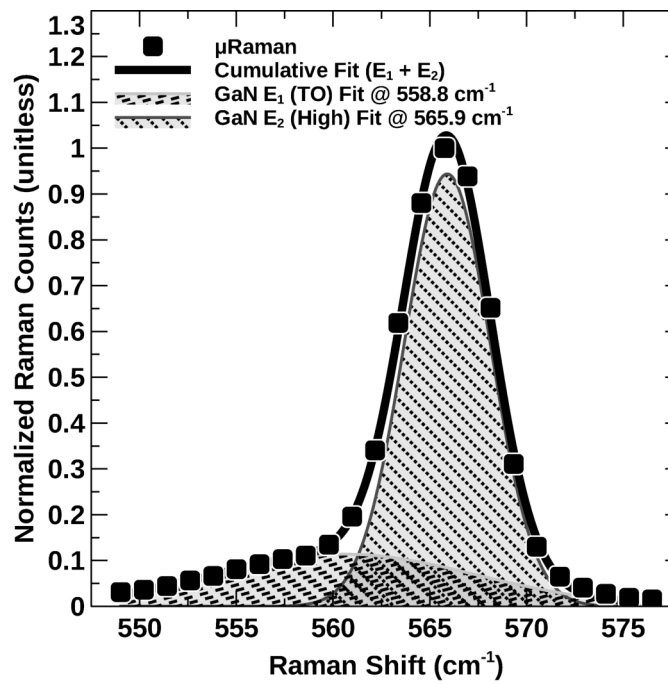


Figure 3.5: Raman spectra were deconvolved into E₂ and E₁ line functions to locate the peak positions of the E₂ mode. One such deconvolution is shown.

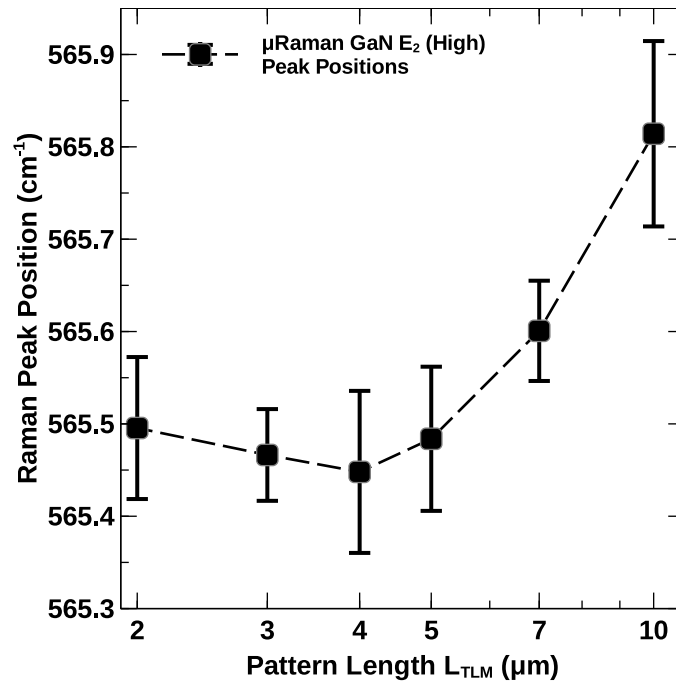


Figure 3.6: E_2 mode peak position measurement results as a function of the pattern length. Error bars represent 99% CI from 10 measurements.

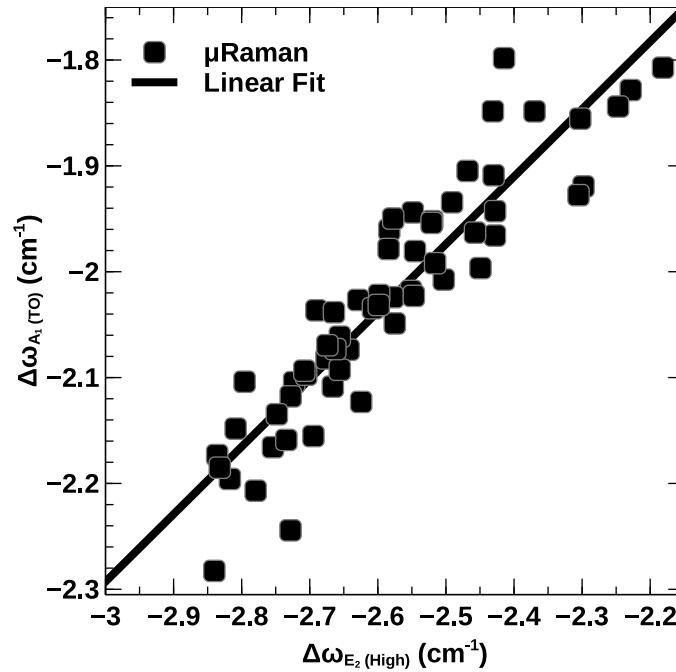


Figure 3.7: Frequency shifts of the E_2 and A_1 modes. Linear fit demonstrated the biaxiality of the measured stress modes.

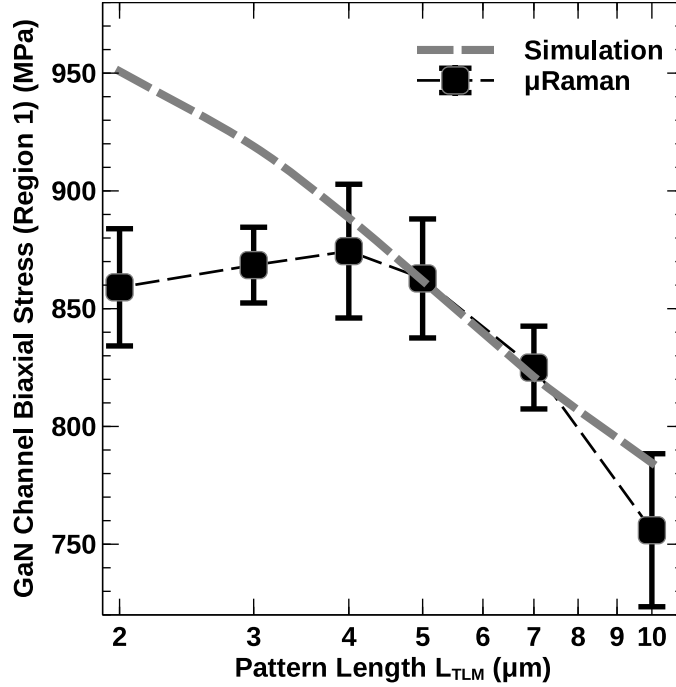


Figure 3.8: Stress measurements and simulation model results. Stresses were calculated from the E_2 peak positions. Error bars represent 99% CI.

we plotted the $\Delta_{A_1}/\Delta_{E_2}$ ratios using the data collected for this work. As shown in Fig. 3.7, the ratios exhibited a linear relation. The slope was determined by a linear least-squares fit to be 0.64, sufficiently close to the 0.69 figure to regard the stress states as biaxial.

3.3 Results and Discussion

3.3.1 Measurement Results and Analysis

Biaxial stresses measured from the center of the ungated HEMT patterns are displayed in Figure 3.8. Error bars represent the 99% CI. We discuss the increasing and decreasing portions separately. The data displays two distinct trends. We start with the upward trend in the stress measurements. The stress increase was limited to the pattern length range of 10 to 4 μm . We believe that the primary contributor to this trend was the

alloyed ohmic contact stress. We suspect that as the contact separation decreased, the influence of the ohmic contact on the channel increased, hence the rise in the measured stresses. Note that in formulating this idea, we disregard the contributions from the 75 nm thick SiN_x layer due to its low intrinsic stress (<100 MPa).

In contrast to the SiN_x layer, ohmic contacts could be under substantial tensile stresses owing to the high temperature (840° C) annealing step. High-temperature procedures may generate significant residual stresses due to the thermal expansion mismatches between the epitaxy and metals. Meng *et al.* investigated ohmic contacts to double channel AlGaIn/GaN HEMTs [46]. They found that high-temperature anneal leads to a considerable volume expansion, thereby tensile stress in the metal film. Whiting *et al.* studied alloyed ohmic contacts on single channel HEMTs [42]. They have proposed that due to (1) material mixings such as nitrogen out-diffusion into the metal stack, (2) gold migration from the metal surface to deeper layers, and (3) aluminum reactions with titanium and gold, large strain fields may form. However, none of the researchers could comment on the precise nature of the stress state and the intrinsic stress value of alloyed ohmic contacts.

Subsequently, we address the observed decreasing trend in the measured data. It is evident that the foregoing discussion does not account for this shift in trend. We, therefore, hypothesize that decreasing the pattern length beyond 4 μm have led to such an increase in stress and/or elastic energy that the devices underwent a defect formation process during the fabrication, which locally relaxed and reduced the stress in the substrate. To verify this argument, we turned our attention to simulations.

3.3.2 Simulation Model Calibration

The foremost goal of the simulation studies was to reproduce the stress measurement results from the ungated HEMTs in an attempt to calibrate the mechanical response of the simulation model to that of the actual device. With a calibrated mechanical model, potential defect-inducing stresses and elastic energies can be reliably identified. A computational model can only be calibrated if a reliable means of comparison methods between the model and measurements are established. First, it is known that GaN

Table 3.2: Values of the stress and strain variables used in the simulation model.

σ_{ohmic}	MPa	750
σ_{res}	GPa	5.0
$\epsilon_{\text{a, AlGaIn}}$	-	0.766%
$\epsilon_{\text{c, AlGaIn}}$	-	-0.402%

is transparent to the green laser used in the Raman experiments. Accordingly, we assumed that the green Raman laser probes the entirety of the GaN substrate. Therefore, the biaxial stress values in the GaN substrate were averaged along the wafer growth direction. Second, to account for the finite size and shape of the Gaussian beam (beam size = 502 nm), we applied a weighted averaging operation to the depth averaged results.

The average stress results from the simulations are displayed in Figure 3.8 alongside the measurements. The simulation model was calibrated to the measurements in the pattern length range of 10 to 4 μm . As explained in Section 2.2.2, the simulation model admitted only two variables, the substrate residual stress and the ohmic contact isotropic stress. To calibrate the model, we set GaN residual stress σ_{res} to 750 MPa. This was because the longest pattern studied in this work ($L_{\text{DS}} = 10 \mu\text{m}$) exhibited an average stress value of about 750 MPa. We assumed that the center of the 10 μm pattern can be assumed to be virtually free of the influence of the ohmic contact stress, thereby manifesting the *true* substrate stress. Strain fields in the barrier were calculated from this residual stress value as described by equations 2.19 to 2.24. It was observed that 5 GPa ohmic stress σ_{ohmic} could explain the upward trend in the stress measurements. Within the calibration range, the results obtained from the simulation model fell within the error bars of the measurements, which demonstrated the success of the calibrated mechanical model. Stress variables and their values are summarized in Table 3.2.

3.3.3 Identifying Potential Defect Generation Spots using the Calibrated Mechanical Model

To verify our hypothesis that decreasing the pattern length beyond $4\ \mu\text{m}$ led to defect generation, we studied the stress and elastic energy distributions within the GaN substrate and AlGaIn barrier. We first used the yield stress metric to identify where mechanical failures might occur in GaN substrate. When a material's yield stress is surpassed, the material is irreversibly deformed. This deformation leads to cracking and dislocation formation, which could subsequently relax and reduce the stress. We note that the yield stress figure is not an exact measure. Material's apparent yield stress is reduced with pre-existing defects, high-temperature processes, and contaminants. Nowak *et al.* studied high-quality GaN samples and reported 15 GPa yield stress [47]. In the analysis of the simulation results, we checked whether stress values in the GaN substrate ever exceeded or became comparable to this value.

To study the AlGaIn barrier, we used the critical thickness (h_{crit}) and critical elastic energy ($U_{\text{crit}}(x,y)$) concepts associated with the pseudomorphic growth of the barrier[48]. These metrics mark the onset of stress relaxation by defect formation. To rephrase, beyond the critical thickness and energy, the barrier can not maintain its large intrinsic strain and instead forms defects to relieve the lattice mismatch stress. The relaxation process is accompanied by cracks and misfit dislocations (MD) [49]. Cracks begin at the barrier surface, run across the thickness of the barrier film, and are initially unconnected. These are called surface cracks. As the elastic energy increases, surface cracks begin to channel. Such cracks grow indefinitely and laterally until they encounter another crack. These cracks are referred to as channeling cracks [50].

To determine which critical thickness measure is relevant to this study, details of the stress relaxation process must be known. For typical Al concentrations encountered in HEMTs ($x < 0.3$), the elastic energy required for MD formation is smaller than what is required for crack generation. Therefore, one could conclude that MDs would enter the barrier first. However, it was observed by several researchers that fully-strained AlGaIn barriers could be grown past the theoretical critical thickness for MD generation [28]. Therefore, it was concluded that defect generation and stress relaxation in the AlGaIn

barrier are crack formation limited. Cracks either provide the nucleation sites for MDs or facilitate MD multiplication. These MD generation processes account for the bulk of stress relaxation [28].

Therefore, in this work, we used the cracking critical thickness measures. These failure mechanisms can be described by the Griffith model [51]. In this model, cracks are generated when the consequent reduction in elastic energy is larger than or equal to creating a new surface due to defects. This model assumes that the material under study is isotropic. This assumption was shown to lead to the overestimation of the critical thickness values by about 10-20%. However, we continue to use the Griffith model, as a complete treatment of the critical thickness is beyond the scope of this work. The critical thickness associated with cracks is expressed by

$$h_{\text{crit}} = \frac{\Gamma}{Z(1 + \nu)M\epsilon_{a, \text{AlGaN}}^2}. \quad (3.2)$$

In this expression, Γ is the fracture resistance, Z is a dimensionless quantity pertaining to a defect's energy release rate, ν is the Poisson ratio, M is the biaxial modulus, and $\epsilon_{a, \text{AlGaN}}$ is the strain of the barrier. As a very simplistic approach, we assume that fracture resistance is purely due to the energy required to create new surfaces for defect generation. In AlGaN, it was observed that cracks occur and create new surfaces along the $\{11\bar{2}0\}$ planes. Accordingly, we set $\Gamma = 2\gamma_{11\bar{2}0}$. For AlGaN $\gamma_{11\bar{2}0}$ is 1.97 J/m^2 [52]. The value of Z is 3.951 for surface cracks and 1.976 for channeling cracks [51]. The values of ν (0.31) and M (460 GPa) were taken from Ref. [49]. The barrier strain $\epsilon_{a, \text{AlGaN}}$ was calculated using Eq. 2.21 to be 0.766%.

The critical elastic energy $U_{\text{crit}}(x, y)$ is the accumulated strain energy (J/m^2) corresponding to a fully strained layer of thickness h_{crit} . This energy is given by $U_{\text{crit}}(x, y) = W_{\text{d}}(x, y, z) \times h_{\text{crit}}$, where $W_{\text{d}}(x, y, z)$ is the elastic energy density in the barrier in J/m^3 . Surface and channeling cracking critical thicknesses were calculated using Eq. 3.2 to be 28.2 and 56.4 nm, respectively. As calculated using simulations, the elastic energy density of the AlGaN barrier was $2.667 \times 10^7 \text{ J/m}^3$. Therefore, the critical elastic energy for surface and channeling cracks were 0.75 and 1.50 J/m^2 , respectively. While analyzing the simulation results, we compared the elastic energy in the barrier with these critical values.

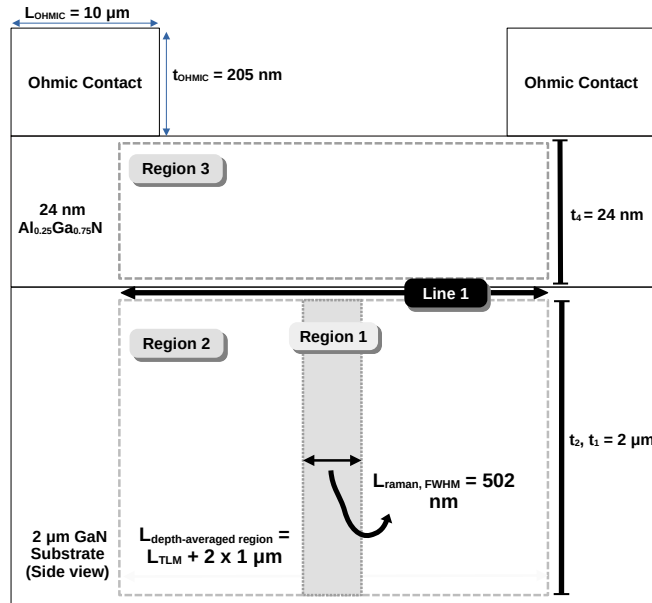


Figure 3.9: Data post-processing regions. Data from Region 1-3 were integrated along the wafer growth direction and reported as line plots. Line 1 represents the line-scan data acquisition 1 nm away from the heterojunction interface.

To analyze stress distributions near and under the ohmic contacts, the x-axes ranges were configured to be $2 \mu\text{m}$ longer than the pattern length L_{DS} . This way, the analysis region protruded $1 \mu\text{m}$ from the channel towards the contacts. The bulk-averaged and near-interface stress distributions were collected from Region 2 and Line 1, as displayed in Figure 3.9, respectively. The near-interface results were collected 1 nm away from the heterojunction interface. Figure 3.10 displays the stress simulation results. The bulk-averaged results in Figure 3.10a revealed that stresses peaked near the contacts, with the exception of 2 micrometers long pattern. Figure 3.10b displays the results obtained from the near-interface region. A more prominent peaking was observed near the contacts. The peaks were as much as two times the center values. Nevertheless, the stress values were far from the reported yield stress limit. Therefore, the stress distributions do not point to a defect generation in the GaN substrate.

Figure 3.11 shows the elastic energy in the barrier. These results were obtained by integrating the elastic energy density in the barrier (Region 3 in Figure 3.9) along the z-axis. Interestingly, the elastic energy in the barrier was either comparable or larger

than the energy required to initiate surface cracking. This result contradicts the findings of references [28, 39]. These previous studies did not consider the substrate's residual stress, which directly influences the barrier lattice constant. On the other hand, our simulation model couples the barrier strain with the residual stress via equations 2.19 to 2.24, thereby offering a more realistic picture of the elastic energies in the barrier. We should note that AlGaIn films can be grown beyond the critical thickness of surface cracking. Therefore, the present data is inconclusive regarding defect generation in the channel region.

Conversely, at the ohmic contact edges, elastic energies were comparable with those required for the formation of channeling cracks. It is important to recall that the critical elastic energy as calculated using equation 3.2 is a 10-20% overestimation due to the isotropy assumption. Taking this overestimation into account, the actual critical energy is as small as 1.2 J/m^2 . This figure could be further lowered due to preexisting defects. Observations from Figure 3.11 reveal that all the patterns under study exhibited elastic energy peaks exceeding 1.20 J/m^2 . This provides substantial grounds to support the notion that stress-relaxing defects could be generated due to the influence of the ohmic contacts, and that these defects would likely form along the ohmic contact edges. Moreover, these defects are likely to manifest themselves as channeling cracks. These channeling cracks would promote MD generation, which in turn would serve to relax local stress. This defect generation picture is consistent with the findings of Whiting *et al.*, who reported the observation of channeling cracks near and under the ohmic contacts, with defects exhibiting depths ranging from 20-30 nm and an average length of approximately 50 nm [42].

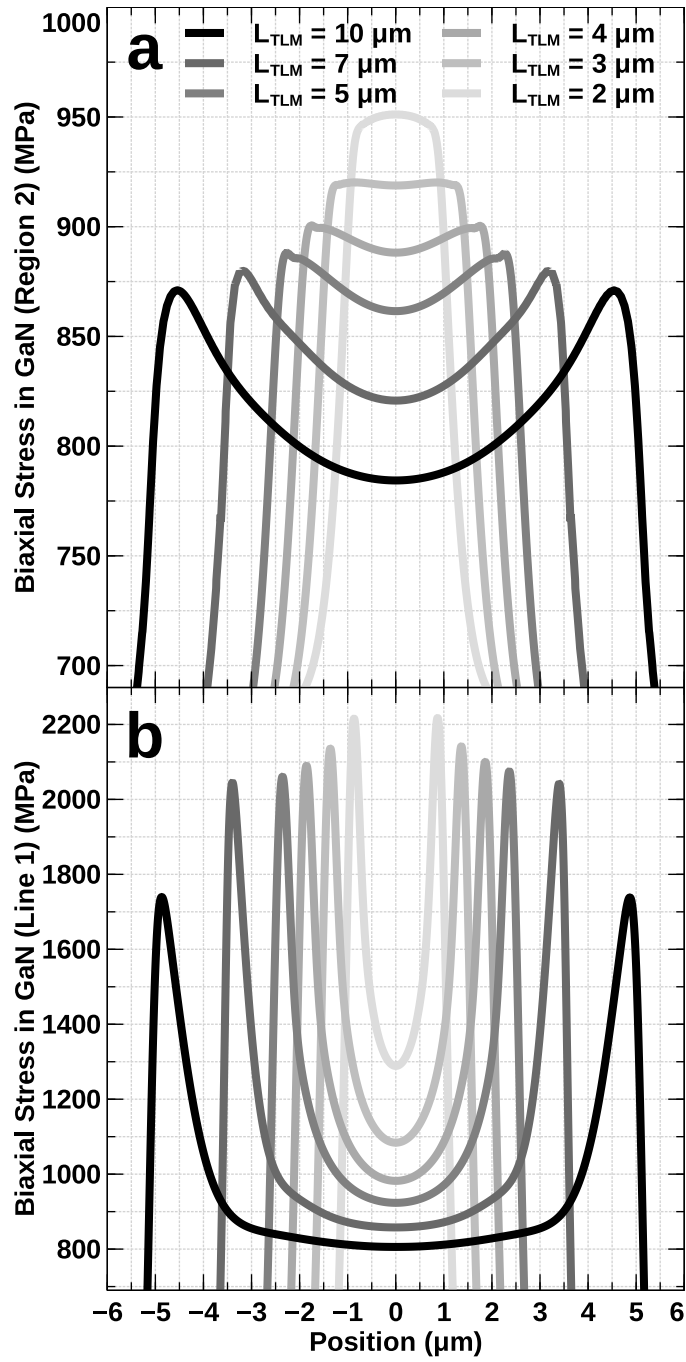


Figure 3.10: Simulation results. Stress results from a) Region 1 and b) Line 1.

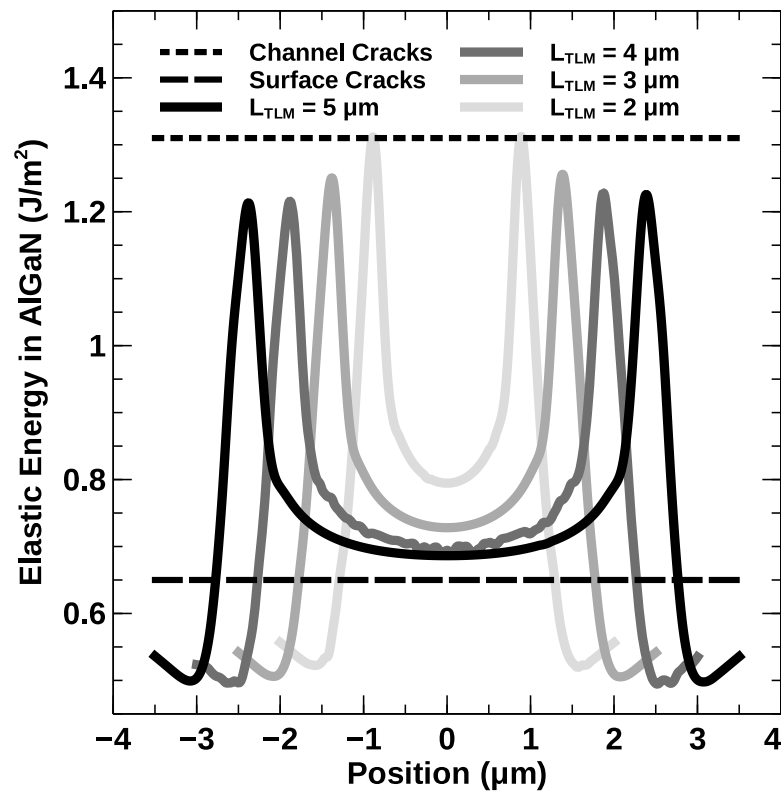


Figure 3.11: Elastic energy in the AlGaN barrier. Energy levels required for the generation of channeling and surface cracks are also given.

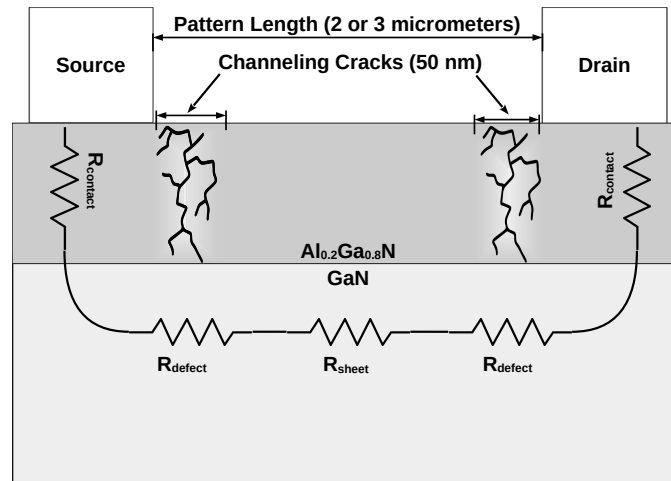


Figure 3.12: A 2D simulation settings illustration depicting channeling cracks near the ohmic contacts.

3.3.4 Impact of Defect Generation on Device Performance

Now that the mechanisms behind defect generation have been explored and found to be in accordance with experimental observations, it is crucial to assess the effects of defect generation on device performance. To this end, electrical simulations were employed to investigate the effects of defect generation along the ohmic contact edges. This was accomplished by emulating the transfer-length method (TLM) [53], a technique employed for measuring ohmic contact resistance and sheet resistivity. The influence of defects was incorporated into the simulations as local strain relaxations in the Al-GaN barrier. For simplicity, it was assumed that cracks are only present in the vicinity of the ohmic contacts and they extend from the contacts towards the channel region. The extent of the relaxation region was set to 50 nm, in conjunction with Whiting's results[42]. The severity of the defect generation and defect density in the vicinity of ohmic contacts was controlled by adjusting the strain relaxation parameter. The density-dependent mobility model of Section 2.1.3 was used. The polarization charge calculation methodology which dictates the relationship between the strain relaxation and polarization charges previously delineated in Section 2.3 was employed. The areas underneath the contacts were modeled as heavily doped regions to give rise to an ohmic behavior. The contact resistance R_c of the ohmic contacts was set to $0.1 \Omega\text{-mm}$. Simulation settings are visualized in Figure 3.12.

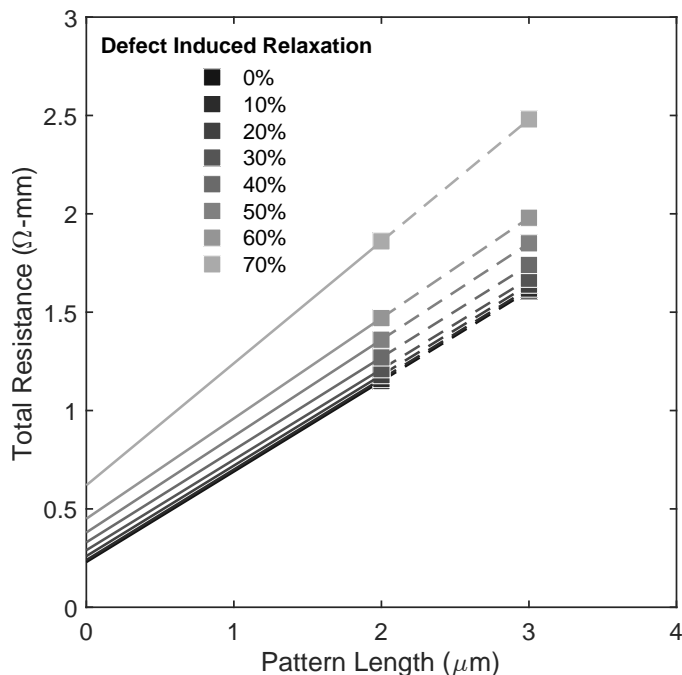


Figure 3.13: TLM emulation results in relation to the severity of defect-induced relaxation

Figure 3.13 presents the TLM measurement simulations along with linear fits, while Figure 3.14 illustrates the extracted contact resistance using the TLM technique. As evident in these figures, the severity of defect generation plays a critical role in influencing the contact resistance, to the extent that the contributions from the defective regions may come to dominantly govern the contact resistance. It is imperative to recognize that this scenario can be further exacerbated if the channeling cracks extend beyond 50 nm. Although at a relatively rare occurrence, Whiting *et al.* observed 600 nm long cracks, which can have even more significant repercussions on the electrical performance of devices [42].

The presented results underline the importance of proper stress monitoring, modeling, and development of low-stress ohmic contact fabrication processes. Fabrication engineers may attempt to counteract the adverse impact of the defect generation by increasing the ohmic contact alloying temperature. An increased temperature could facilitate the metal inclusion into the epitaxy, increase nitrogen vacancy generation efficiency, and reduce the apparent ohmic contact resistance [54, 55, 56, 57, 58]. While this might improve the ohmic contact resistance and transistor transfer characteristics,

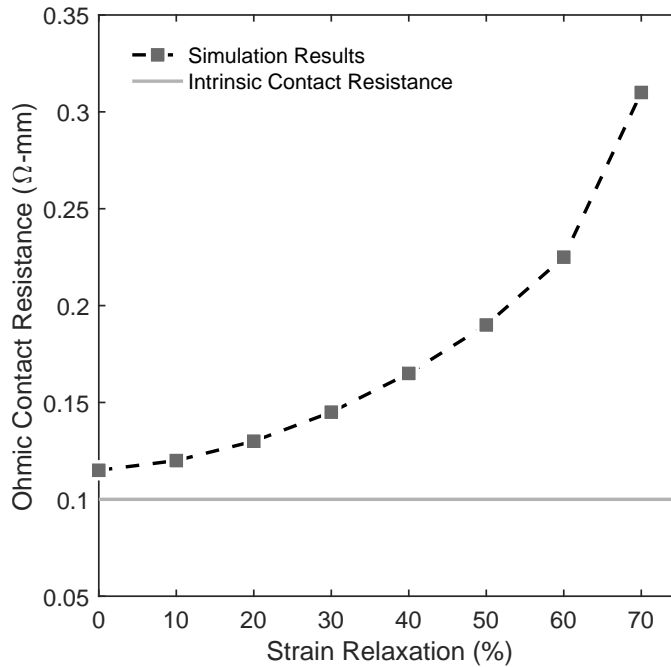


Figure 3.14: Extracted contact resistances from the emulated TLM results.

such an approach could inadvertently damage the surface of the barrier by inducing a preferential nitrogen loss [59, 60], thereby adversely impacting the 2DEG mobility as well as device reliability and repeatability. The surface damage can be alleviated or prevented by introducing surface reinforcement layers such as a thin layer of SiN_x with the purpose of protecting the AlGaIn surface during the high temperature alloying phase [59]. However, these approaches would increase the complexity of the fabrication process, and may introduce new challenges in terms of material compatibility, process integration, and cost-effectiveness.

3.4 Summary

Mechanical properties of ungated HEMTs were studied with simulations and Raman measurements. Raman results demonstrated two distinct stress trends. The upward trend was explained by the influence of the ohmic contact stress on the channel region. The downward trend was thought to result from a defect generation that locally relaxed and reduced the stress. A simulation model was developed to justify this hypothesis.

This simulation model was calibrated to the upward trend in the measurements. Calibration was accomplished by adjusting the residual stress in the GaN substrate and stress in the ohmic contacts. Lattice mismatch strain in the barrier was calculated from the residual stress in the substrate. Simulation results were compared with yield stress and theoretical critical energies for crack generation. Simulations showed that GaN substrate was unlikely to exhibit yielding. However, the substantial elastic energy build-up in the barrier could initiate channeling crack formation, especially near and under ohmic contacts. These cracks would then facilitate MD formation processes, reducing the barrier's stress and elastic energy. Finally, this study emphasized the necessity of stress and strain analysis by shedding light on how defects can adversely influence fundamental performance metrics such as the ohmic contact resistance.

Chapter 4

Improved Drain Lag by Reduced Surface Current in GaN HEMT via an Ultrathin HfO₂ Blanket Layer

This section is a reproduction of the communication "Improved drain lag by reduced surface current in GaN HEMT via an ultrathin HfO₂ blanket layer", B. Güneş, A. Ghobadi, O. Odabasi, B. Bütün, E. Özbay, *Semiconductor Science and Technology*, vol. 38, no. 6, p. 065002, Apr. 2023. doi:10.1088/1361-6641/accc4e. This work was published under the Creative Commons Attribution 4.0 International licence (CC BY 4.0), which entitles the authors to freely disseminate their work.

4.1 Motivation

Gallium nitride based high-electron-mobility transistors (HEMTs) are afflicted by trapping-induced current dispersions [61]. Upon recovering from their off-states with a non-zero drain potential, HEMTs display a severe reduction of the drain current, which is called drain lag. This lagging behavior lowers the radio-frequency (RF) power output substantially [61, 62, 63, 64]. The dominant mechanism of drain lag is trapping on

the surface above the drain access region [61]. Filled traps deplete the 2DEG channel, increase the channel resistance, and shift the threshold voltage.

Drain lag can be mitigated by inserting gate dielectrics. For example, Hove *et al.* showed that a $\text{Si}_3\text{N}_4(10 \text{ nm})/\text{Al}_2\text{O}_3(5 \text{ nm})$ gate dielectric stack can suppress drain lag [65]. Similarly, Anand *et al.* studied an $\text{Al}_2\text{O}_3(5 \text{ nm})/\text{Si}_3\text{N}_4(5 \text{ nm})$ gate dielectric stack and achieved a similar improvement [66]. However, thick gate dielectrics produce devices with highly reduced transconductances due to the increased gate-to-channel spacing [67]. Also, thick gate dielectrics lead to a significant threshold hysteresis due to bulk traps residing within the dielectrics [68].

Besides these adverse impacts the gate dielectrics have on the IV characteristics, thick dielectrics also present structural instability issues. For example, HfO_2 and Al_2O_3 layers show poly-crystallization at temperatures as low as $500 \text{ }^\circ\text{C}$ and $600 \text{ }^\circ\text{C}$, respectively [69]. Poly-crystal films are not desirable as they are less reproducible, less uniform, and exhibit higher leakage currents compared to amorphous layers [70]. Solid phase transitions are especially worrisome in the case of GaN HEMTs, which experience temperatures of up to $900 \text{ }^\circ\text{C}$ during fabrication and show peak hot-spot temperatures of around $250 \text{ }^\circ\text{C}$ during nominal operation. These issues ultimately limit the commercialization of MOS-HEMT and MIS-HEMT devices.

On the other hand, ultrathin films have the potential to alleviate these problems while offering prominent improvements over the Schottky-gate design. Thin atomic-layer-deposition (ALD) layers are thermodynamically more stable and less likely to exhibit phase transitions under thermal cycling [70]. Also, bulk trap densities associated with thin layers are usually smaller. In general, the first few ALD cycles passivate the semiconductor surface, while subsequent ALD cycles increase bulk trap densities [71]. For example, Sim *et al.* investigated the impact of ALD HfO_2 thickness on silicon field effect transistors. They reported that transistors with 1.8 nm thick gate dielectric exhibited the least threshold voltage instability compared to the transistors with 2.5 nm and 3.3 nm films [72]. Similarly, Kim *et al.* studied ALD AlN layers on GaN. They noted that trap densities of the 7.4 nm thick AlN layer were four times that of the 1.5 nm layer, while both samples displayed similar leakage characteristics [73]. Therefore, downscaling the gate dielectric thickness can be a promising compromise

for improving transistor threshold stability, reliability characteristics, and transconductance.

Existing research on ALD ultrathin gate dielectrics for AlGaIn/GaN HEMTs is rather limited. For example, Yue *et al.* studied a 3.5 nm Al₂O₃ gate dielectric [74]. Zhory *et al.* demonstrated a 5 nm thick SiN_x plasma enhanced ALD (PEALD) layer on recessed GaN HEMTs [75]. To demonstrate further downscaling of the GaN HEMT gate dielectrics, we studied a 1.5 nm thick gate dielectric. To the best of our knowledge, this work represents the thinnest ALD gate dielectric study on AlGaIn/GaN HEMTs. The 1.5 nm film thickness choice is motivated as follows: In an earlier study, we investigated ultrathin ALD HfO₂ film growth characteristics over a crystalline host (TiO₂). We observed that ALD HfO₂ deposition exhibited the typical traits of the island growth mode [76]. We also discovered that full surface coverage, conformality, and island coalescence could only be obtained after 15 ALD cycles, corresponding to a film thickness of 1.5 nm as measured by transmission electron microscopy (results not shown). In light of this experiment, we opted to limit the downscaling of the gate dielectric to 1.5 nm.

In this work, we decided to employ HfO₂ as a gate dielectric material to demonstrate the benefits of the ultrathin approach. Nevertheless, we believe that our approach is material system independent. As explained above, susceptibility to solid phase transitions and increase in the bulk trap densities is known to increase with dielectric thickness regardless of the material. On the other hand, there are several reasons why we decided on HfO₂ to demonstrate this technology. First, using HfO₂ as an ultrathin layer is attractive from a reliability point of view. HfO₂ is a dense material and can suppress gate metal electromigration and oxygen diffusion into the epitaxy and produce more reliable devices [77]. HfO₂ exhibits a large conduction band offset with AlGaIn, which helps reduce gate leakage [78]. Gao *et al.* showed that adsorbed water moisture on the AlGaIn barrier exacerbates the current collapse phenomenon [79]. HfO₂ is known to exhibit hydrophobic surface properties [80]. Hydrophobicity could reduce the surface sensitivity of the GaN HEMTs and help fabricate more stable devices. Finally, HfO₂ is a high-k dielectric and does not significantly reduce the device transconductance.

This paper studied the influence of an ultrathin (1.5 nm) HfO₂ gate dielectric on

GaN HEMTs. The HfO₂ deposition before the gate metallization reduced the electron injection into surface states near the gate contact. Manufactured devices exhibited a highly suppressed drain lag behavior, superior leakage, turn-on, and linearity characteristics than those without the HfO₂ application. No degradation of the IV properties was observed.

4.2 Device Fabrication

The Fe-doped AlGa_xN/GaN epitaxial structure was grown on a 3" 4H-SiC substrate by metal-organic chemical vapor deposition (MOCVD). The barrier structure consisted of a 10 Å AlN spike, a 20 nm Al_{0.28}Ga_{0.72}N, and a 3 nm GaN cap layer. Fabrication was commenced with the ohmic contact patterning by optical lithography. Then, a Ti/Al/Ni/Au stack was deposited via electron-beam evaporation and annealed in an N₂ environment at 840°C for 30 s. Following a Cl₂ based 100 nm mesa etch, a 75 nm silicon nitride passivation layer (SiN_x) was deposited in a plasma-enhanced chemical-vapor-deposition system (PECVD). After the SiN_x passivation layer deposition, e-beam lithography was used to define the T-gate foot regions. Then, the SiN_x was selectively dry-etched in the foot regions. Subsequently, one set of the devices received the 1.5 nm HfO₂ film by ALD using tetrakis dimethylamino-hafnium and deionized water as precursors at 250°C. After the HfO₂ deposition, both samples were annealed at 450°C for 10 minutes in N₂. Following the annealing step, T-gate head regions were defined using e-beam lithography, and a Ni/Au gate stack was deposited using e-beam evaporation. Finally, samples were annealed at 400°C for 30 s in N₂ for Schottky interface stabilization. The device cross-section and design dimensions are outlined in Figure 4.1a. The process flow is displayed in Figure 4.1b. Figure 4.2 shows the simulated conduction band energy diagram of the gate stacks. Band diagram calculations were carried out in Silvaco ATLAS [11]. The band alignment parameters between HfO₂ and GaN were taken from the literature [81]. As shown in Figure 4.2, HfO₂ deposition increases the barrier height for electrons and can effectively reduce the electron injection into the epitaxy.

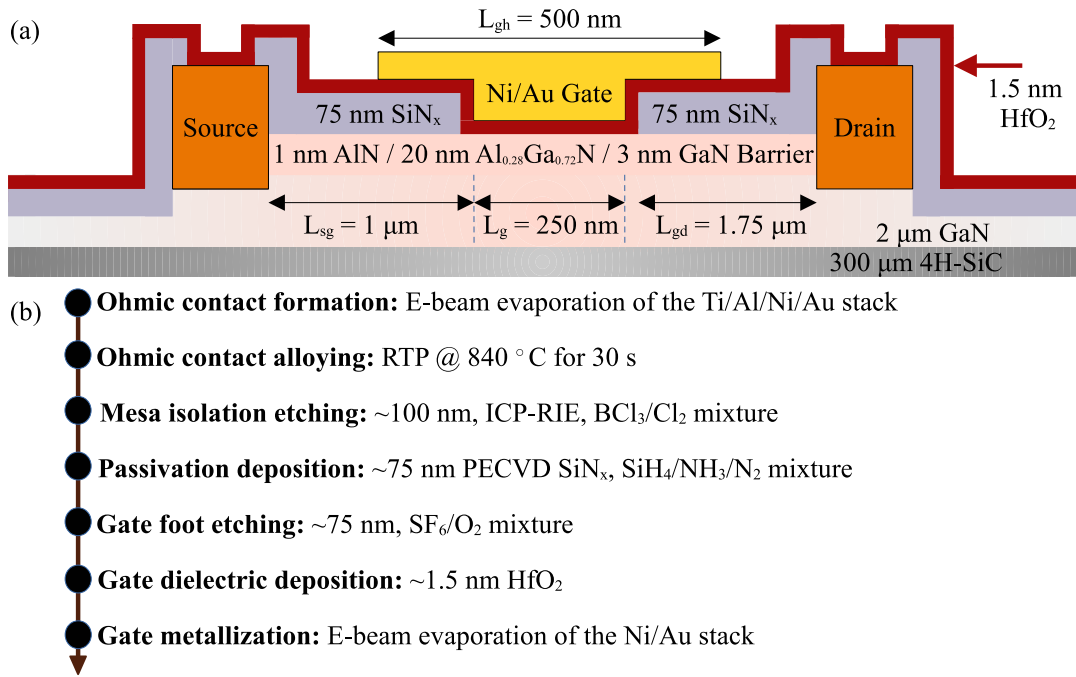


Figure 4.1: (a) Cross-section of the HEMTs (the reference sample is absent of the HfO₂ layer). (b) Simplified fabrication flow.

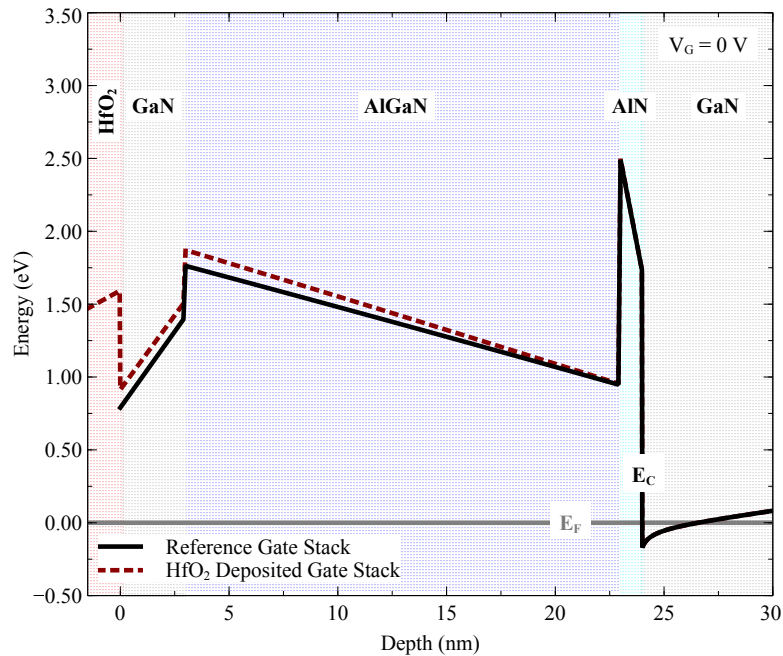


Figure 4.2: Calculated conduction band diagram of the AlGaN/GaN HEMT gate stacks with and without the HfO₂ dielectric.

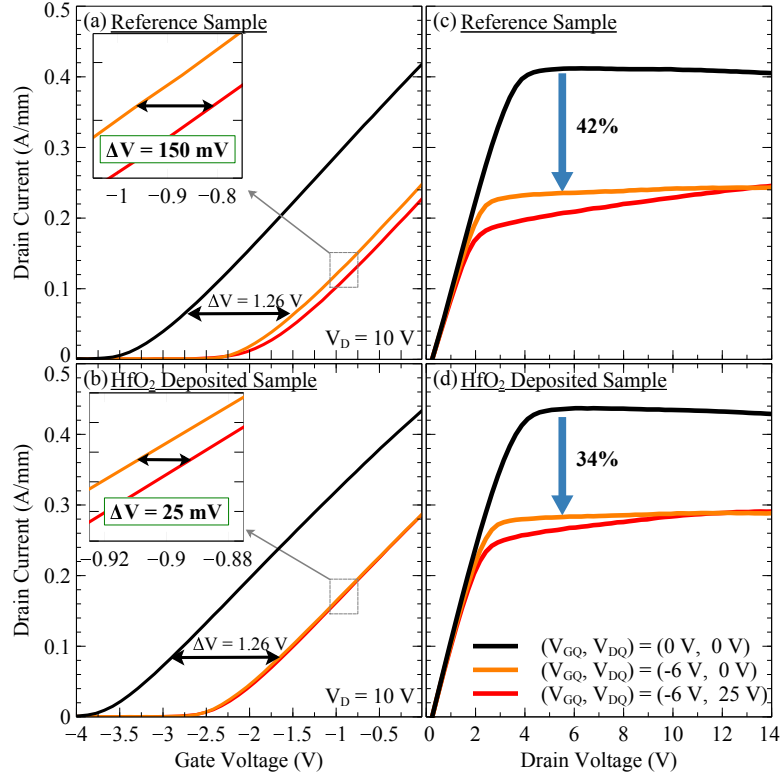


Figure 4.3: Double pulsed measurement results. Insets of (a) and (b) show the drain lag results in close-up.

4.3 Results and Discussion

Double-pulsed measurements were taken to analyze the trapping behavior under and near the gate. Quiescent voltages were set to $(V_{GQ1}, V_{DQ1}) = (-6 \text{ V}, 0 \text{ V})$ and $(V_{GQ2}, V_{DQ2}) = (-6 \text{ V}, 25 \text{ V})$, respectively, for gate and drain lag. The pulse width was $500 \mu\text{s}$, and the duty cycle was 0.1% to effectively fill the traps. Figures 4.3a and 4.3b show the measurement results at $V_D = 10 \text{ V}$. Figures 4.3c and 4.3d show the pulsed I_D - V_D measurement results. The pulsed I_D - V_G measurements reveal the suppression of the drain-lag-induced threshold shift. The reference transistor exhibited a 150 mV threshold shift after the drain lag stress, whereas the HfO_2 deposited sample only showed a 25 mV shift. Both samples displayed an identical gate lag response, indicating that the devices equally suffered from trapping underneath the gate caused by bulk trap states in the barrier. These traps can not be passivated with surface modifications; therefore, they are not of interest in the present study.

Dielectric	Deposition Method	Thickness (nm)	Gate Length (μm)	Peak g_m Drop (%)	Hysteresis (mV)	I_g Reduction	Ref
Al_2O_3	ALD	3.5	0.80	11.7	Not given	10^2	[74]
SiN_x	PEALD	5.0	0.25	Not given	100	10^3	[75]
$\text{Al}_2\text{O}_3/\text{HfO}_2$	ALD	3.0/2.0	1.00	9.1	Not given	10^1	[86]
$\text{Al}_2\text{O}_3/\text{SiN}_x$	ALD	5.0/5.0	0.30	1.6	200	10^1	[66]
HfO_2	ALD	1.5	0.25	5.0	Negligible	10^2	This work

Table 4.1: Comparisons of MIS-HEMTs and MOS-HEMTs with the conventional Schottky-gate AlGaIn/GaN HEMTs.

Next, the drain lag suppression mechanism was investigated by surface conduction measurements. In the virtual gate model, the trap states on the barrier surface are filled with electrons upon electron injection from the gate electrode. This trap filling action depletes the channel near the gate electrode and shifts the threshold voltage [61]. Therefore, surface leakage correlates well with the drain lag performance [82]. Surface current was measured by adopting the approach by Tan *et al.* with a gate-to-gate distance (L_{gg}) of $5 \mu\text{m}$ [82]. Figure 4.4a and 4.4b shows the cross-sectional view of the devices used in the surface conduction measurements. Figure 4.5a displays the results. The surface current is reduced by about three orders of magnitude, which is in close correlation with the drain lag improvement. These results are consistent with earlier reports on SiN_x passivation in the literature, i.e., as the HfO_2 film surrounds the gate metal, it reduced electron conduction to the traps on the drain access region and improved both the leakage characteristics and drain lag performance [82]. Similarly, Liu *et al.* investigated 10 nm ALD Al_2O_3 blanket layers and achieved a comparable improvement in the surface current [83]. This comparable improvement albeit the difference in the film thicknesses might be because thicker films may support additional lateral conduction mechanisms. Grain boundary formations in thick polycrystalline ALD films introduce parasitic conduction paths, usually via variants of Poole-Frenkel and trap-assisted tunneling mechanisms [84, 85]. Since the HfO_2 film studied in this work is only 1.5 nm thick, polycrystalline grain formation and associated conduction mechanisms could be inhibited, thereby improving the surface leakage characteristics. However, more work is needed to confirm this argument.

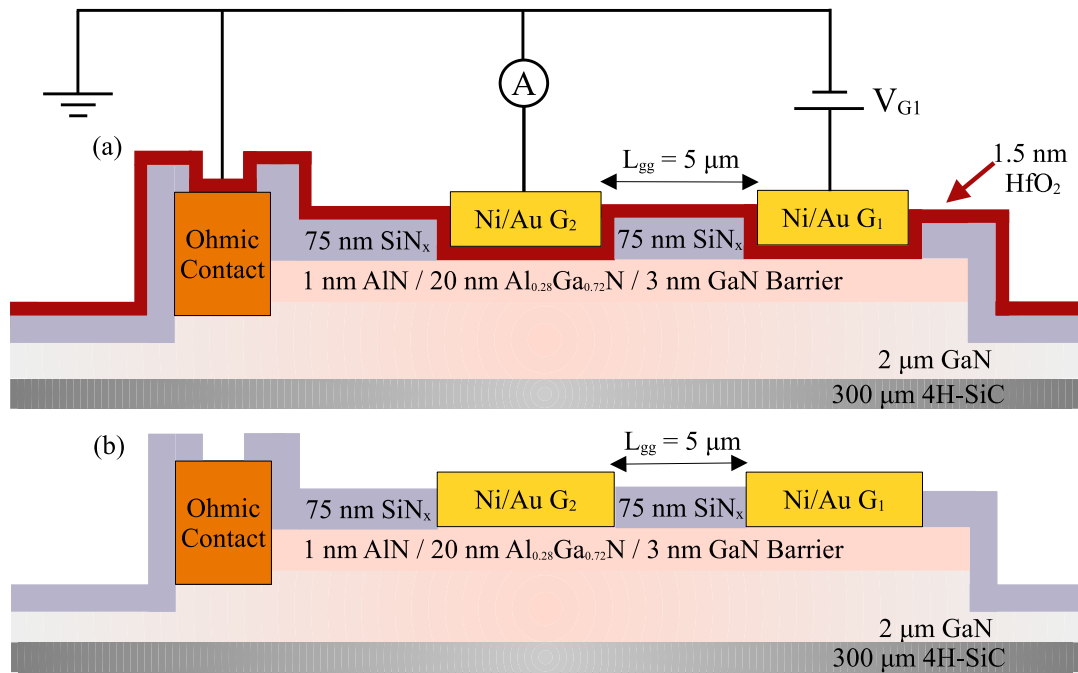


Figure 4.4: (a) and (b) display the cross-section of the devices used in the surface leakage current measurements. (a) also shows the measurement circuit for surface leakage current.

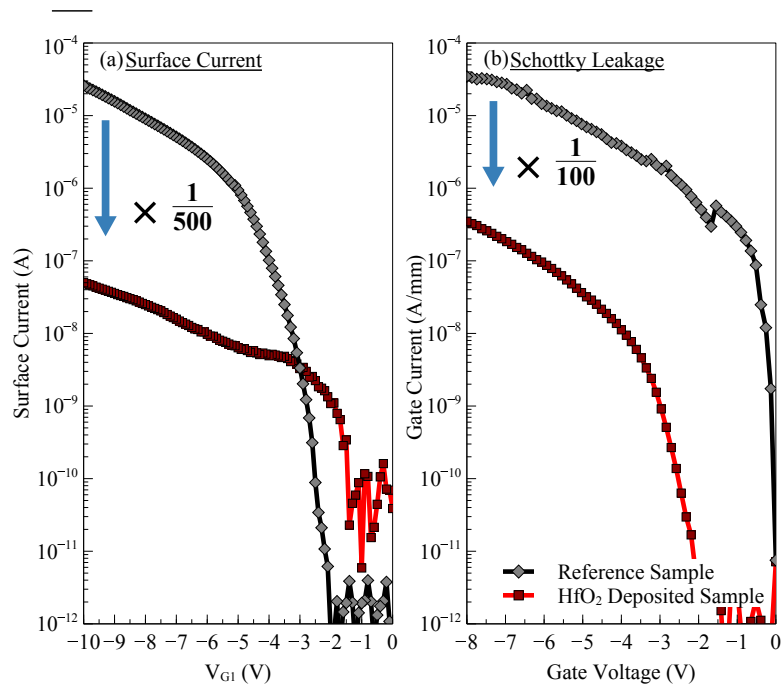


Figure 4.5: (a) Surface current measurement results. (b) Schottky leakage measurement results from the HEMTs.

To verify the proper operation of transistors, Schottky leakage (Figure 4.5b) and two-way I_D - V_G and I_G - V_G (Figures 4.6a and b) measurements were conducted. Schottky leakage results display two orders of magnitude decrease. This reduction is owing to the large conduction band difference between HfO_2 and GaN [81]. As summarized in Table 4.1, this improvement in the gate leakage is comparable to or even better than some of the reported work on thicker gate dielectrics. Two-way measurements show that both samples exhibited negligible counter-clockwise hysteresis, indicating that trapping in the oxide was insignificant [68]. Table 4.1 verifies the view that bulk traps in the thick dielectrics lead to an inferior threshold voltage stability performance. Also, the HfO_2 deposited transistor delivered better turn-on characteristics, as evidenced by the reduced subthreshold slope of 94 mV/dec at $V_D = 0.1$ V due to the leakage reduction [87]. Figure 4.7a shows the V_D - I_D transfer characteristics and Figure 4.7b displays the transconductance of the transistors. The HfO_2 and reference samples exhibited saturation currents of 0.440 A/mm and 0.400 A/mm, and 154 and 162 mS/mm peak transconductances at $V_D = 10$ V, respectively. The observed difference in the drain current between the two transistors can be explained by the shift in the threshold voltage. Specifically, the negatively shifted threshold voltage in the HfO_2 deposited transistor suggests a higher electron density underneath the gate electrode compared to the reference device. This increased electron density reduces the intrinsic resistance of the transistor, resulting in a higher drain current. Thus, the shift in the threshold voltage is likely the primary cause of the observed difference in the drain current. Also, as expected, the ultrathin high-k HfO_2 film insertion did not significantly degrade the transconductance (only 5% reduction) [67]. This drop is almost negligible compared to transconductance losses of the thicker dielectric insertion attempts (see table 4.1).

The off-state breakdown characteristics of the transistors were studied to understand the impact of the HfO_2 layer on gate electrostatics. The drain current was limited to 2 mA/mm during the breakdown measurements to avoid catastrophic damage, in a similar fashion to the references [88] and [89]. The drain voltage at which this current limit was attained was determined to be the breakdown voltage. The results are displayed in Figure 4.8. The devices exhibited a soft-breakdown behavior within the studied drain voltage range, which indicates a poor depletion of electrons despite the pinching-off of the channel. This is an expected behavior as the gate length is only 250 nm, which

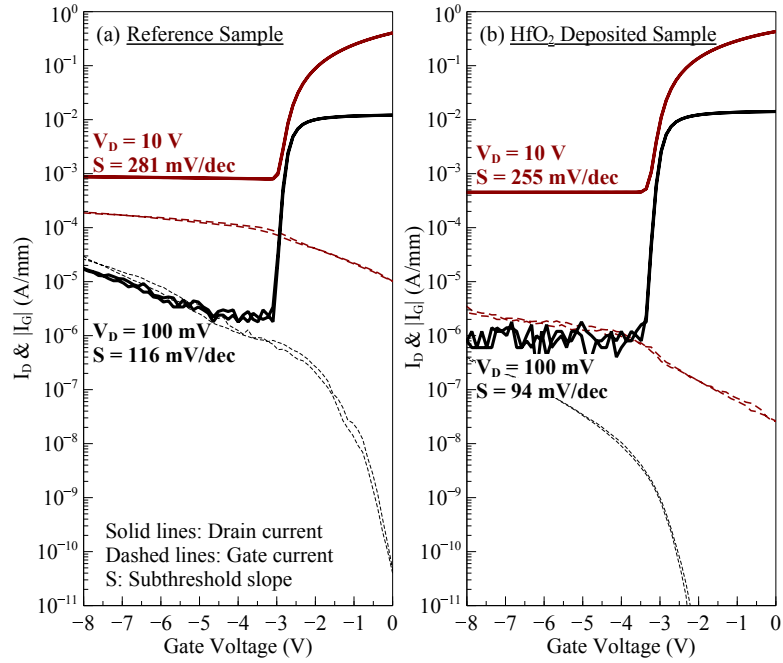


Figure 4.6: (a) and (b) are the two-way I_D - V_G and I_G - V_G results of the transistors.

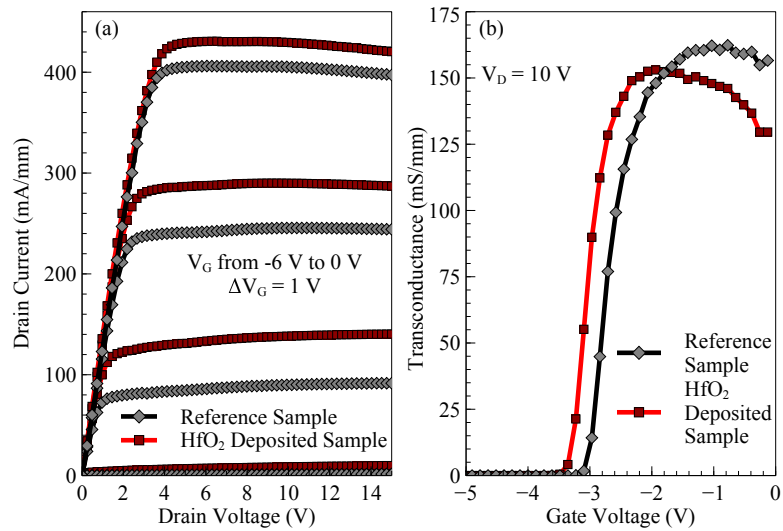


Figure 4.7: (a) I_D - V_D sweep at gate voltages ranging from -6 V to 0 V with 1 V steps. (b) Transconductance g_m at $V_D = 10$ V.

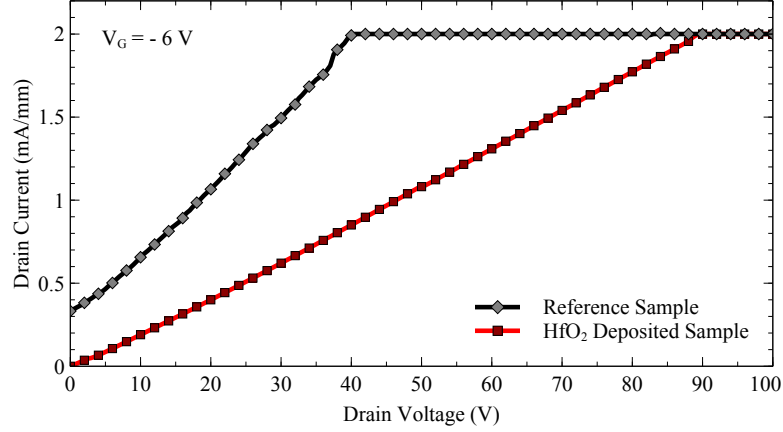


Figure 4.8: Current-controlled I_D - V_D measurements.

makes the devices susceptible to short-channel effects such as punch-through [88]. On the other hand, the HfO_2 sample demonstrated an 88 V off-state breakdown voltage at $V_G = -6$ V, two times that of the reference transistor, which is a clear improvement compared to the conventional HEMT. Ohno *et al.* investigated the influence of surface passivation on the breakdown performance and found that the suppression of electron trapping at the surface relieves the high electric field formation in the drain access region and improves the breakdown characteristics [90]. In parallel with Ohno's findings, we believe that the suppression of surface trapping by the reduced surface current improved the gate electrostatics and, consequently, the breakdown behavior.

The conductance method was adopted to study the HfO_2 film quality [91]. Parallel capacitance-conductance measurements were taken over the frequency range 10kHz to 1MHz. Figure 4.9 shows the conductance method results. Trap density was calculated by fitting $G_p/\omega = q\omega\tau_{it}D_{it}(1 + (\omega\tau_{it})^2)^{-1}$ to the calculated G_p/ω curves, where q is the elementary charge, ω is the radial measurement frequency, D_{it} is the trap density, and τ_{it} is the trap time constant [53]. The calculations were carried out under the assumptions of discontinuum of trap energy levels (as opposed to a trap continuum near the interface) and negligible series resistance. The trap density results are given in Figure 4.10a. Our trap density results are compatible with the literature [78, 92]. The HfO_2 deposited sample showed an as much as 60% reduction in the trap density within the studied range, demonstrating the quality of the HfO_2 -GaN interface. This trap density reduction suggests that the HfO_2 film was able to passivate a significant

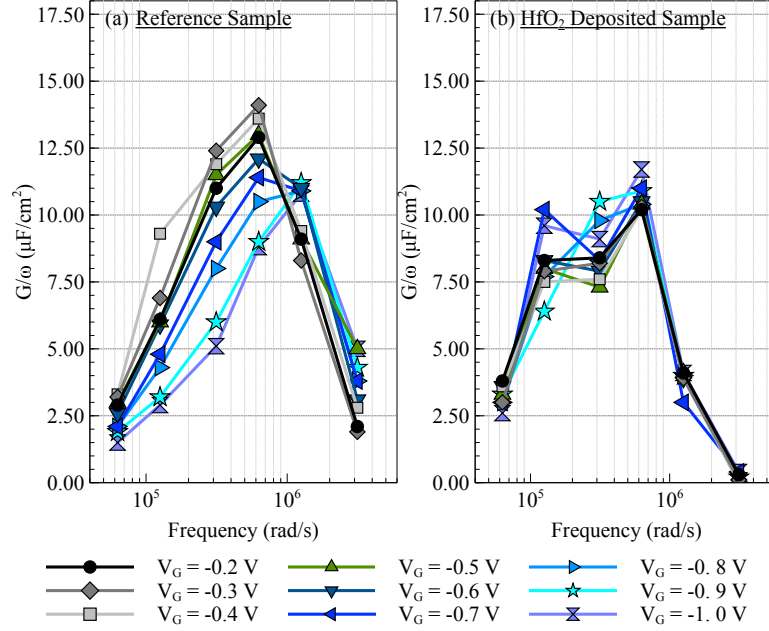


Figure 4.9: Conductance method results.

portion of the surface traps. Figure 4.10b shows the extracted trap time constants τ_{it} using the conductance method. The trap lifetimes of the HfO_2 deposited sample were approximately $3 \mu\text{s}$, which is 50% more than the reference sample's trap lifetimes. This could be due to the formation of HfON and GaON bonds at the interface [93].

Small-signal measurements were taken over the frequency range 0.4-28 GHz at various gate biases (Figure 4.11). The pad parasitics were not de-embedded. The peak f_T dropped by approximately 5% due to the reduced transconductance. Linearity was evaluated by defining a gate voltage swing (GVS) parameter corresponding to the values larger than 95% of the peak f_T . Linearity improved by 16%, corresponding to a GVS span of 1.86 V. This improvement can be understood quantitatively by referring to the governing equations of the small-signal regime. As a first-order approximation, f_T is $1/2\pi\tau_{int}$ where τ_{int} is the total time for electrons to go across the confines of the gate electrode. Under the influence of drain bias, τ_{int} must be replaced with $\tau_{tot} = \tau_{int} + \tau_{drain}$, where τ_{drain} accounts for the spreading of the effective gate length [67]. We propose that HfO_2 deposition has reduced the variations in τ_{drain} by hindering the electron flow to the surface, thereby limiting the lateral reach of the gate depletion region, thereby improving the gate electrostatics and linearity. However, this argument

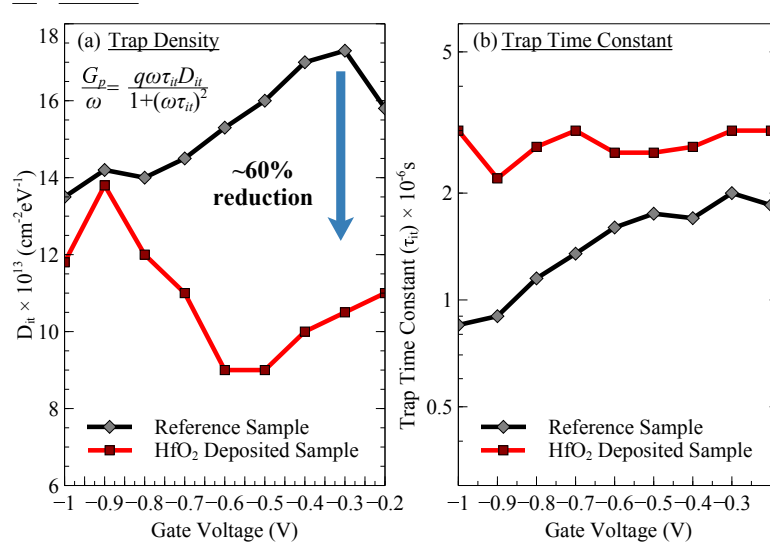


Figure 4.10: (a) The calculated interface trap density and (b) time constant evolution with gate voltage.

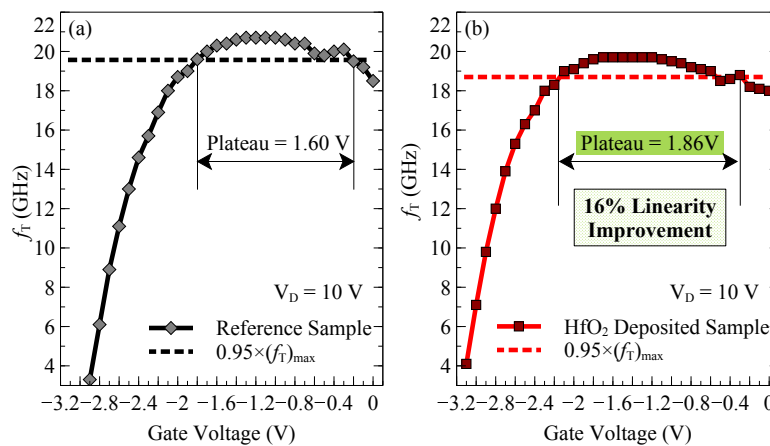


Figure 4.11: f_T as a function of gate bias at a fixed drain voltage of 10 V of (a) the reference and (b) HfO₂ deposited transistors.

is not yet conclusive and warrants further investigation.

4.4 Summary

Blanket deposition of a 1.5 nm thin HfO₂ layer shows a remarkable success in suppressing drain lag. HfO₂ dielectric hampers lateral conduction of electrons injected from the gate contact, reduces trapping on the device surface, and does not degrade the transistor transport properties. The proposed manufacturing technique is readily applicable to the conventional GaN HEMT fabrication processes, requiring only one additional step with no lithography.

Chapter 5

Conclusions and Future Work

The research problems tackled in this thesis revolved around understanding and improving the reliability and fabrication processes of GaN HEMTs. By using Raman measurements as calibration benchmarks in simulations, we have analyzed stress distributions in very fine detail. This approach has shed new light on how these stresses contribute to defect generation and, in turn, influence the electrical characteristics of GaN HEMTs. Furthermore, we have discovered that introducing an ultrathin film shows promise for reducing drain lag, offering a practical compromise that does not significantly degrade other electrical properties. While this study has yielded important insights into device behavior and performance, several limitations of the proposed studies must be acknowledged.

1. Regarding the development of the electro-mechanical model, it must be noted that there has been a lack of thorough verification. Future work must engage in comprehensive validation studies.
2. The proposed density-dependent mobility model, although promising in its results, requires additional validation. A broader range of case studies need to be examined to ensure the model's universality. Furthermore, the impact of temperature on the model remains an unexplored area.
3. The Raman study could benefit from more extensive experimental validation as

well, particularly with respect to defect generation modes and the observation of channeling cracks.

4. The use of HfO_2 necessitates further research, especially on ultrathin film reliability. The current study saw considerable improvements in device performance. However, the reliability of ultrathin films under operational conditions remains uncertain. In addition, despite the noted improvements, the trap density remains significant.

Next, we discuss potential avenues for future research, building on the methodologies developed in this work. We anticipate that these suggested future studies will further enhance our understanding of GaN HEMTs.

Simulation-based Statistical Analysis

The density-dependent models could lay the foundation for extensive simulation-based statistical analyses. This research path could lead to the development of robust statistical models, beneficial for analyzing fabrication yield and performance variability. Crucial questions such as, "How does the deviation in barrier thickness across the wafer (± 1 nm) influence the IV and RF characteristics?" and "What is the impact of gate length variation on RF performance?" can be addressed. Such analyses are commonly employed in the CMOS industry, both to improve fabrication processes and to reduce the impact of process variability on integrated circuit design.

Design of FinHEMTs Using the Uncoupled Electro-mechanical Model

The uncoupled electro-mechanical model along with the density-dependent mobility approach developed in this research has potential applications in the design of FinHEMTs. Leveraging these models, future work could optimize the performance of

FinHEMTs, taking into account and exploiting the inherent coupling between mechanical and electrical characteristics.

Bibliography

- [1] U. Mishra, P. Parikh, and Y.-F. Wu, “AlGaN/GaN HEMTs—an overview of device operation and applications,” *Proceedings of the IEEE*, vol. 90, no. 6, pp. 1022–1031, 2002.
- [2] O. Ambacher, B. Foutz, J. Smart, J. Shealy, N. Weimann, K. Chu, M. Murphy, A. Sireakowski, W. Schaff, L. Estman, R. Dimitrov, A. Mitchell, and M. Stutzmann, “Two dimensional electron gases induced by spontaneous and piezoelectric polarization in undoped and doped AlGa_N/Ga_N heterostructures,” *Journal of Applied Physics*, vol. 87, pp. 334–344, January 2000.
- [3] J. Davies, *The Physics of Low-dimensional Semiconductors: An Introduction*. Cambridge University Press, 1998.
- [4] R. Fitch, D. Walker, A. Green, S. Tetlak, J. Gillespie, R. Gilbert, A. K. Sutherlin, W. Gouty, J. Theimer, and G. Jessen, “Implementation of High-Power-Density X-Band AlGa_N/Ga_N High Electron Mobility Transistors in a Millimeter-Wave Monolithic Microwave Integrated Circuit Process,” *IEEE Electron Device Letters*, vol. 36, pp. 1004–1006, October 2015.
- [5] Y. Zhang, S. Huang, K. Wei, S. Zhang, X. Wang, Y. Zheng, G. Liu, X. Chen, Y. Li, and X. Liu, “Millimeter-Wave AlGa_N/Ga_N HEMTs With 43.6/Power-Added-Efficiency at 40 GHz Fabricated by Atomic Layer Etching Gate Recess,” *IEEE Electron Device Letters*, vol. 41, pp. 701–703, May 2020.
- [6] O. Jardel, M. Olivier, D. Lancereau, R. Aubry, E. Chartier, N. Sarazin, M.-A. Di Forte Poisson, S. Piotrowicz, M. Stanislawiak, D. Rimbart, S. Delage, and

- P. Eudeline, "A 30W, 46applications," in *2012 7th European Microwave Integrated Circuit Conference*, pp. 639–642, 2012.
- [7] T. Y. K. Shinohara, D. Regan, A. Corrion, D. Brown, J. Wong, A. Schmitz, H. Fung, S. Kim, and M. Micovic, "Ultrahigh-Speed GaN High-Electron-Mobility Transistors With f_T / f_{max} of 454/444 GHz," *IEEE Electron Device Letters*, vol. 36, pp. 549–552, June 2015.
- [8] M. Uren, J. Möreke, and M. Kuball, "Buffer Design to Minimize Current Collapse in GaN/AlGaN HFETs," *IEEE Transactions on Electron Devices*, vol. 59, pp. 3327–3333, December 2012.
- [9] F. Gao, D. Chen, H. L. Tuller, C. V. Thompson, and T. Palacios, "On the redox origin of surface trapping in AlGaN/GaN high electron mobility transistors," *Journal of Applied Physics*, vol. 115, p. 124506, 03 2014.
- [10] E. Dreyer, A. Janotti, C. G. Van de Walle, and D. Vanderbilt, "Correct Implementation of Polarization Constants in Wurtzite Materials and Impact on III-Nitrides," *Physical Review X*, vol. 6, p. 021038, 2016.
- [11] Silvaco, Inc., "ATLAS User's Manual," 2020.
- [12] Silvaco, Inc., "ATHENA User's Manual," 2020.
- [13] B. Rackauskas, M. J. Uren, S. Stoffels, M. Zhao, S. Decoutere, and M. Kuball, "Determination of the Self-Compensation Ratio of Carbon in AlGaN for HEMTs," *IEEE Transactions on Electron Devices*, vol. 65, no. 5, pp. 1838–1842, 2018.
- [14] I. Rossetto, D. Bisi, C. de Santi, A. Stocco, G. Meneghesso, E. Zanoni, and M. Meneghini, *Performance-Limiting Traps in GaN-Based HEMTs: From Native Defects to Common Impurities*, pp. 197–236. Cham: Springer International Publishing, 2017.
- [15] J. L. Lyons, D. Wickramaratne, and C. G. Van de Walle, "A first-principles understanding of point defects and impurities in GaN," *Journal of Applied Physics*, vol. 129, p. 111101, 03 2021.

- [16] K. Sagisaka, O. Custance, N. Ishida, T. Nakamura, and Y. Koide, "Identification of a nitrogen vacancy in GaN by scanning probe microscopy," *Phys. Rev. B*, vol. 106, p. 115309, Sep 2022.
- [17] M. G. Ganchenkova and R. M. Nieminen, "Nitrogen Vacancies as Major Point Defects in Gallium Nitride," *Phys. Rev. Lett.*, vol. 96, p. 196402, May 2006.
- [18] M. Pinto, C. Rafferty, and R. Dutton, *PISCES II: Poisson and Continuity Equation Solver*. Stanford University, September 1984.
- [19] M. J. Uren and M. Kuball, "Impact of carbon in the buffer on power switching GaN-on-Si and RF GaN-on-SiC HEMTs," *Japanese Journal of Applied Physics*, vol. 60, p. SB0802, feb 2021.
- [20] M. Uren, K. Nash, R. Balmer, T. Martin, E. Morvan, N. Caillas, S. Delage, D. Ducatteau, B. Grimbert, and J. De Jaeger, "Punch-through in short-channel AlGaN/GaN HFETs," *IEEE Transactions on Electron Devices*, vol. 53, no. 2, pp. 395–398, 2006.
- [21] G. Meneghesso, M. Meneghini, and E. Zanoni, "Breakdown mechanisms in AlGaN/GaN HEMTs: An overview," *Japanese Journal of Applied Physics*, vol. 53, p. 100211, sep 2014.
- [22] D. Caughey and R. Thomas, "Carrier mobilities in silicon empirically related to doping and field," *Proceedings of the IEEE*, vol. 55, no. 12, pp. 2192–2193, 1967.
- [23] S. Bajaj, O. F. Shoron, P. S. Park, S. Krishnamoorthy, F. Akyol, T.-H. Hung, S. Reza, E. M. Chumbes, J. Khurgin, and S. Rajan, "Density-dependent electron transport and precise modeling of GaN high electron mobility transistors," *Applied Physics Letters*, vol. 107, p. 153504, 10 2015.
- [24] D. F. Brown, A. Williams, K. Shinohara, A. Kurdoghlian, I. Milosavljevic, P. Hashimoto, R. Grabar, S. Burnham, C. Butler, P. Willadsen, and M. Miovic, "W-band power performance of AlGaN/GaN DHFETs with regrown n+ GaN ohmic contacts by MBE," in *2011 International Electron Devices Meeting*, pp. 19.3.1–19.3.4, 2011.

- [25] V. Kumar, A. Kuliev, R. Schwindt, M. Muir, G. Simin, J. Yang, M. Asif Khan, and I. Adesida, “High performance 0.25 μm gate-length AlGaIn/GaN HEMTs on sapphire with power density of over 4.5 W/mm at 20 GHz,” *Solid-State Electronics*, vol. 47, no. 9, pp. 1577–1580, 2003.
- [26] COMSOL, Inc., Burlington, MA 01803 USA, *COMSOL Multiphysics*.
- [27] A. Wright, “Elastic properties of zinc-blende and wurtzite AlN, GaN and InN,” *Journal of Applied Physics*, vol. 82, pp. 2833–2839, June 1997.
- [28] M. Auf der Maur and A. Di Carlo, “AlGaIn/GaN HEMT Degradation: An Electro-Thermo-Mechanical Simulation,” *IEEE Transactions on Electron Devices*, vol. 60, pp. 3142–3148, October 2013.
- [29] “Derivation of the rule of mixtures and inverse rule of mixtures,” July 2023.
- [30] S. Choi, E. Heller, D. Dorsey, R. Vetry, and S. Graham, “Analysis of the residual stress distribution in AlGaIn/GaN high electron mobility transistors,” *Journal of Applied Physics*, vol. 113, p. 093510, 2013.
- [31] S. L. Chuang, *Physics of Optoelectronic Devices*. John Wiley and Sons, Inc., 1995.
- [32] Y. Sun, S. Thompson, and T. Nishida, *Strain Effects in Semiconductors*. Springer, 2010.
- [33] Y. Zhang, A. Zubair, X. M. Liu, Z. and, J. Perozek, Y. Ma, and T. Palacios, “GaN FinFETs and trigate devices for power and RF applications: review and perspective,” *Semiconductor Science and Technology*, vol. 36, p. 054001, March 2021.
- [34] J. Khurhin, S. Bajaj, and S. Rajan, “Amplified spontaneous emission of phonons as a likely mechanism for density-dependent velocity saturation in GaN transistors,” *Applied Physics Express*, vol. 9, p. 094101, July 2016.
- [35] T. Fang, R. Wang, H. Xing, S. Rajan, and D. Jena, “Effect of Optical Phonon Scattering on the Performance of GaN Transistors,” *IEEE Electron Device Letters*, vol. 33, pp. 709–711, May 2012.

- [36] E. Sermeksnis, J. Liberis, M. Ramonas, A. Matulionis, J. Leach, M. Wu, V. Avrutin, and H. Morkoç, “Camelback channel for fast decay of LO phonons in GaN heterostructure field-effect transistor at high electron density,” *Applied Physics Letters*, vol. 99, p. 043501, 2011.
- [37] G. Meneghesso, G. Verzellesi, F. Danesin, F. Rampazzo, F. Zanon, A. Tazzoli, M. Meneghini, and E. Zanoni, “Reliability of GaN High-Electron-Mobility Transistors: State of the Art and Perspectives,” *IEEE Transactions on Device and Materials Reliability*, vol. 8, no. 2, pp. 332–343, 2008.
- [38] M. Silvestri, M. Uren, and M. Kuball, “Dynamic Transconductance Dispersion Characterization of Channel Hot-Carrier Stressed 0.25 micrometer AlGaIn/GaN HEMTs,” *IEEE Electron Device Lett.*, vol. 33, pp. 1550–1552, November 2012.
- [39] J. Joh, F. Gao, T. Palacios, and J. Alamo, “A model for the critical voltage for electrical degradation of GaN high electron mobility transistors,” *Microelectronics Reliability*, vol. 50, pp. 767–773, June 2010.
- [40] *The Impact of Defects on GaN Device Behavior: Modeling Dislocations, Traps, and Pits*, vol. 5, ECS, 2016.
- [41] F. Gao, S. C. Tan, J. A. del Alamo, C. V. Thompson, and T. Palacios, “Impact of Water-Assisted Electrochemical Reactions on the OFF-State Degradation of AlGaIn/GaN HEMTs,” *IEEE Transactions on Electron Devices*, vol. 61, pp. 437–444, July 2014.
- [42] P. Whiting, N. Rudawski, M. Holzworth, S. Pearton, K. Jones, L. Liu, T. Kang, and F. Ren, “Nanocrack formation in AlGaIn/GaN high electron mobility transistors utilizing Ti/Al/Ni/Au ohmic contacts,” *Microelectronics Reliability*, vol. 70, pp. 41–48, February 2017.
- [43] M. Kuball, “Raman spectroscopy of GaN, AlGaIn and AlN for process and growth monitoring/control,” *Surface and Interface Analysis*, vol. 31, pp. 987–999, 2001.
- [44] E. Saloman, “Wavelengths, Energy Level Classifications, and Energy Levels for the Spectrum of Neutral Mercury,” *J. Phys. Chem. Ref. Data*, vol. 35, no. 4, pp. 1519–1548, 2006.

- [45] M. Azize and T. Palacios, "Top-down fabrication of AlGaIn/GaN nanoribbons," *Applied Physics Letters*, vol. 98, p. 042103, 2011.
- [46] Q. Meng, Q. Lin, W. Jing, P. Yang, and D. Lu, "Investigation on the Effect of Annealing Temperature on the Side Ohmic Contact Characteristics for Double Channel GaN/AlGaIn Epitaxial Layer," *micromachines*, vol. 13, p. 791, 2022.
- [47] R. Nowak, M. Pessa, M. Suganuma, M. Leszczynski, I. Grzegory, S. Porowski, and F. Yoshida, "Elastic and plastic properties of GaN determined by nano-indentation of bulk crystal Elastic and plastic properties of GaN determined by nano-indentation of bulk crystal," *Applied Physics Letters*, vol. 75, pp. 2070–2072, October 1999.
- [48] S. Lee, D. Koleske, K. Cross, J. Floro, K. Waldrip, A. Wise, and S. Mahajan, "In situ measurements of the critical thickness for strain relaxation in heterostructures," *Applied Physics Letters*, vol. 85, pp. 6164–6167, December 2004.
- [49] J. Floro, D. Follstaedt, P. Provencio, S. Hearne, and S. Lee, "MISFIT dislocation formation in the AlGaIn/GaN heterointerface," *Journal of Applied Physics*, vol. 96, no. 12, pp. 7087–7094, 2004.
- [50] J. Vlassak, "Channel cracking in thin films on substrates of finite thickness," *International Journal of Fracture*, vol. 119, pp. 299–323, 2003.
- [51] J. Hutchinson and Z. Suo, "Mixed Mode Cracking in Layered Materials," *Advances in Applied Mechanics*, vol. 29, pp. 63–191, 1992.
- [52] S. Hearne, J. Han, S. Lee, J. Floro, D. Follstaedt, E. Chason, and I. Tsong, "Brittle-ductile relaxation kinetics of strained AlGaIn/GaN heterostructures," *Applied Physics Letters*, vol. 76, pp. 1534–1537, March 2000.
- [53] D. K. Schroder, *Semiconductor Material and Device Characterization*. Wiley, 2006.
- [54] R. Gong, J. Wang, Z. Dong, S. Liu, M. Yu, C. Wen, Y. Hao, B. Shen, Y. Cai, B. Zhang, and J. Zhang, "Analysis on the new mechanisms of low resistance stacked Ti/Al Ohmic contact structure on AlGaIn/GaN HEMTs," *Journal of Physics D: Applied Physics*, vol. 43, p. 395192, September 2010.

- [55] L. Wang, F. Mohammed, and I. Adesida, "Formation mechanism of Ohmic contacts on AlGa_N/Ga_N heterostructure: Electrical and microstructural characterizations," *Journal of Applied Physics*, vol. 103, p. 093516, May 2008.
- [56] X. Kong, G. Liu, and X. Liu, "Role of Ti/Al relative thickness in the formation mechanism of Ti/Al/Ni/Au Ohmic contacts to AlGa_N/Ga_N heterostructures," *Journal of Physics D: Applied Physics*, vol. 45, p. 265101, June 2012.
- [57] A. Graff, M. Smion-Najasek, F. Altmann, J. Kuzmik, D. Gregusova, S. Hascik, H. Jung, T. Baur, J. Grünenpütt, and H. Blanck, "High resolution physical analysis of ohmic contact formation at Ga_N HEMT devices," *Microelectronics Reliability*, vol. 76-77, pp. 338–343, July 2017.
- [58] B. Van Daele, G. Tendeloo, W. Ruythooren, J. Derluyn, M. Leys, and M. Germain, "The role of Al on Ohmic contact formation on n-type Ga_N and AlGa_N/Ga_N," *Applied Physics Letters*, vol. 87, p. 061905, August 2005.
- [59] J. Derluyn, S. Boeykens, K. Cheng, R. Vandersmissen, J. Das, W. Ruythooren, S. Degroote, M. Leys, M. Germain, and G. Borghs, "Improvement of AlGa_N/Ga_N high electron mobility transistor structures by in situ deposition of a Si₃N₄ surface layer," *Journal of Applied Physics*, vol. 98, p. 054501, September 2005.
- [60] A. Zhang, G. Dang, F. Ren, J. Van Hove, J. Klaassen, P. Chow, X. Cao, and S. Pearton, "Effect of N₂ discharge treatment on AlGa_N/Ga_N high electron mobility transistor ohmic contacts using inductively coupled plasma," *Journal of Vacuum Science and Technology*, vol. 18, pp. 1149–1152, August 2000.
- [61] R. Vetury, N. Q. Zhang, S. Keller, and U. K. Mishra, "The impact of surface states on the DC and RF characteristics of AlGa_N/Ga_N HFETs," *IEEE Trans. Electron Devices*, vol. 48, pp. 560–566, 2001.
- [62] J. M. Tirado, J. L. Sanchez-Rojas, and J. I. Izpura, "Trapping Effects in the Transient Response of AlGa_N/Ga_N HEMT Devices," *IEEE Trans. Electron Devices*, vol. 54, pp. 410–417, 2007.

- [63] S. H. Y. Zhang and, K. Wei, S. Zhang, X. Wang, Y. Zheng, G. Liu, X. Chen, Y. Li, and X. Liu, “Millimeter-Wave AlGaIn/GaN HEMTs With 43.6 Power-Added-Efficiency at 40 GHz Fabricated by Atomic Layer Etching Gate Recess,” *IEEE Electron Device Lett.*, vol. 41, pp. 701–704, 2020.
- [64] H. Du, J. Zhang, H. Zhou, Z. Liu, T. Zhang, Y. Zhang, W. Zhang, Y. Zhang, and Y. Hao, “GaN High-Electron-Mobility-Transistor on Free- Standing GaN Substrate With Low Contact Resistance and State-of-the-Art $f_T \times LG$ Value,” *IEEE Trans. Electron Devices.*, vol. 69, pp. 968–972, 2022.
- [65] M. V. Hove, X. Kang, S. Stoffels, D. Wellekens, N. Ronchi, R. Venegas, K. Geens, and S. Decoutere, “Fabrication and Performance of Au-Free AlGaIn/GaN-on-Silicon Power Devices With Al_2O_3 and Si_3N_4/Al_2O_3 Gate Dielectrics,” *IEEE Trans. Electron Devices*, vol. 60, pp. 3071–3078, 2013.
- [66] M. J. Anand, G. I. Ng, S. Vicknesh, S. Arulkumaran, and K. Ranjan, “Reduction of current collapse in AlGaIn/GaN MISHEMT with bilayer SiN/ Al_2O_3 dielectric gate stack,” *phys. stat. sol. (c)*, vol. 10, pp. 1421–1425, 2013.
- [67] H. Morkoç, *Nitride Semiconductor Devices: Fundamentals and Applications*. Wiley, 2013.
- [68] O. I. Saadat and T. Palacios in *2011 Proceedings of the European Solid-State Device Research Conference (ESSDERC)*, (Helsinki), pp. 287–290, IEEE.
- [69] H. N. Masten, J. D. Phillips, , and R. L. Peterson, “Effects of high temperature annealing on the atomic layer deposited HfO_2/β - $Ga_2O_3(010)$ interface,” *J. Appl. Phys.*, vol. 131, p. 035106, 2022.
- [70] V. Miikkulainen, M. Leskelä, M. Ritala, and R. L. Puurunen, “Crystallinity of inorganic films grown by atomic layer deposition: Overview and general trends ,” *J. Appl. Phys.*, vol. 113, p. 021301, 2013.
- [71] T. G. Ulusoy, A. Ghobadi, and A. K. Okyay, “Surface engineered angstrom thick ZnO-sheathed TiO_2 nanowires as photoanodes for performance enhanced dye-sensitized solar cells,” *J. Mater. Chem. A*, vol. 2, pp. 16867–16876, 2014.

- [72] J. Sim, S. Song, P. Kirsch, C. Young, R. Choi, D. Kwong, B. Lee, and G. Bersuker, "Effects of ALD HfO₂ thickness on charge trapping and mobility," *Microelectron. Eng.*, vol. 80, pp. 218–221, 2005.
- [73] H. Kim, H. Yoon, and B. Choi, "Thickness Dependence on Interfacial and Electrical Properties in Atomic Layer Deposited AlN on c-plane GaN," *Nanoscale Res. Lett.*, vol. 13, p. 232, 2018.
- [74] Y. Yuan-Zheng, H. Yue, F. Qian, Z. Jin-Cheng, M. Xiao-Hua, and N. Jin-Yu, "GaN MOS-HEMT Using Ultra-Thin Al₂O₃ Dielectric Grown by Atomic Layer Deposition," *Chin. Phys. Lett.*, vol. 24, pp. 2419–2422, 2007.
- [75] S. Zhang, X. Liu, K. Wei, S. Huang, X. Chen, Y. Zhang, Y. Zheng, G. Liu, T. Yuan, X. Wang, H. Yin, Y. Yao, and J. Niu, "Suppression of Gate Leakage Current in Ka-Band AlGaIn/GaN HEMT With 5-nm SiN Gate Dielectric Grown by Plasma-Enhanced ALD," *IEEE Trans. Electron Devices.*, vol. 68, pp. 49–52, 2021.
- [76] R. Puurunena and W. Vandervorst, "Island growth as a growth mode in atomic layer deposition: A phenomenological model," *J. Appl. Phys.*, vol. 96, p. 7686, 2004.
- [77] Z. Gao, M. F. Romero, and F. Calle, "Thermal and Electrical Stability Assessment of AlGaIn/GaN Metal-Oxide-Semiconductor High-Electron Mobility Transistors (MOS-HEMTs) With HfO₂ Gate Dielectric," *IEEE Trans. Electron Devices*, vol. 65, pp. 3142–3148, 2018.
- [78] X. Qin, L. Cheng, S. McDonnell, A. Azcatl, H. Zhu, J. Kim, and R. Wallace, "A comparative study of atomic layer deposition of Al₂O₃ and HfO₂ on AlGaIn/GaN," *J Mater Sci: Mater Electron*, vol. 26, pp. 4638–4643, 2015.
- [79] F. Gao, D. Chen, H. Tuller, C. Thompson, and T. Palacios, "On the redox origin of surface trapping in AlGaIn/GaN high electron mobility transistors," *J. Appl. Phys.*, vol. 115, p. 124506, 2014.
- [80] R. Martín-Palma and C. Pantano, "Ultra-thin hafnium oxide coatings grown by atomic layer deposition: hydrophobicity/hydrophilicity over time," *Mater. Res. Express*, vol. 6, p. 086457, 2019.

- [81] J. Gong, Z. Zheng, D. Vincent, J. Zhou, J. Kim, D. Kim, T. Ng, B. Ooi, K. Chen, and Z. Ma, "Interfacial band parameters of ultrathin ALD- Al_2O_3 , ALD- HfO_2 , and PEALD- $\text{AlN}/\text{ALD-}\text{Al}_2\text{O}_3$ on c-plane, Ga-face GaN through XPS measurements," *J. Appl. Phys.*, vol. 132, p. 135302, 2022.
- [82] W. S. Tan, M. J. Uren, P. A. Houston, R. T. Green, R. S. Balmer, and T. Martin, "Surface leakage currents in SiN_x passivated AlGaN/GaN HFETs," *IEEE Electron Device Lett.*, vol. 27, pp. 1–3, 2006.
- [83] Z. H. Liu, G. I. Ng, H. Zhou, S. Arulkumaran, and Y. K. T. Maung, "Reduced surface leakage current and trapping effects in AlGaN/GaN high electron mobility transistors on silicon with $\text{SiN}/\text{Al}_2\text{O}_3$ passivation," *Appl. Phys. Lett.*, vol. 98, p. 113506, 2011.
- [84] M. Spechta, M. Stadale, S. Jakschik, and U. Schröder, "Transport mechanisms in atomic-layer-deposited Al_2O_3 dielectrics," *Appl. Phys. Lett.*, vol. 84, p. 3076, 2004.
- [85] C. Tanner, Y. Perng, C. Frewin, S. Sadow, and J. Chang, "Electrical performance of Al_2O_3 gate dielectric films deposited by atomic layer deposition on 4H-SiC," *Appl. Phys. Lett.*, vol. 91, p. 203510, 2007.
- [86] Y. Yue, Y. Hao, J. Zhang, J. Ni, W. Mao, Q. Feng, and L. Liu, "AlGaN/GaN MOS-HEMT With HfO_2 Dielectric and Al_2O_3 Interfacial Passivation Layer Grown by Atomic Layer Deposition," *IEEE Electron Device Lett.*, vol. 29, pp. 838–840, 2008.
- [87] J. W. Chung, J. C. Roberts, E. L. Piner, and T. Palacios, "Effect of Gate Leakage in the Subthreshold Characteristics of AlGaN/GaN HEMTs," *IEEE Electron Device Lett.*, vol. 29, pp. 1196–1198, 2008.
- [88] G. Meneghesso, M. Meneghini, and E. Zanoni, "Breakdown mechanisms in AlGaN/GaN HEMTs: An overview," *Jpn J Appl Phys*, vol. 53, pp. 100211–8, 2014.
- [89] B. Green, K. Chu, E. Chumbes, J. Smart, J. Shealy, and L. Eastman, "The effect of surface passivation on the microwave characteristics of undoped AlGaN/GaN HEMTs," *IEEE Electron Device Lett.*, vol. 21, pp. 268–270, 2000.

- [90] Y. Ohno, T. Nakao, S. Kishimoto, and K. Maezawa, "Effects of surface passivation on breakdown of AlGaIn/GaN high-electron-mobility transistors," *Appl. Phys. Lett.*, vol. 84, pp. 2184–6, 2004.
- [91] E. H. Nicollian and A. Goetzberger, "The si-sio₂ interface – electrical properties as determined by the metal-insulator-silicon conductance technique," *Bell Syst. Tech. Jour.*, vol. 46, p. 243503, 1967.
- [92] X. Ma, J. Zhu, X. Liao, T. Yue, W. Chen, and Y. Hao, "Quantitative characterization of interface traps in Al₂O₃/AlGaIn/GaN metal-oxide-semiconductor high-electron-mobility transistors by dynamic capacitance dispersion technique," *Appl. Phys. Lett.*, vol. 103, p. 033510, 2013.
- [93] Y. Chang, M. Huang, Y. Chang, Y. Lee, H. Chiu, J. Kwo, and M. Hong, "Atomic-layer-deposited Al₂O₃ and HfO₂ on GaN: A comparative study on interfaces and electrical characteristics," *Micr. Engi.*, vol. 77, pp. 1207–1210, 2011.